ADVANCING EARTH AND SPACE SCIENCE

JGR Atmospheres

RESEARCH ARTICLE

10.1029/2021JD035764

# Global Atmospheric OCS Trend Analysis From 22 NDACC Stations

**James W. Hannigan[1], Ivan Ortega[1], Shima Bahramvash Shams[1], Thomas Blumenstock[2], John Elliott Campbell[3], Stephanie Conway[4], Victoria Flood[4], Omaira Garcia[5], David Griffith[6], Michel Grutter[7], Frank Hase[2], Pascal Jeseck[8], Nicholas Jones[9], Emmanuel Mahieu[10], Maria Makarova[11], Martine De Mazière[12], Isamu Morino[13], Isao Murata[14], Toomo Nagahama[15], Hideaki Nakijima[13], Justus Notholt[16], Mathias Palm[16], Anatoliy Poberovskii[11], Markus Rettinger[17], John Robinson[18], Amelie N. Röhling[2], Matthias Schneider[2], Christian Servais[10], Dan Smale[18], Wolfgang Stremme[7], Kimberly Strong[4], Ralf Sussmann[17], Yao Te[8], Corinne Vigouroux[12], and Tyler Wizenberg[4]**

[1]Atmospheric Chemistry, Observations & Modeling, National Center for Atmospheric Research, Boulder, CO, USA, [2]Karlsruhe Institute of Technology, Institute of Meteorology and Climate Research (IMK-ASF), Karlsruhe, Germany, [3]Department of Environmental Studies, University of California, Santa Cruz, CA, USA, [4]Department of Physics, University of Toronto, Toronto, ON, Canada, [5]Izaña Atmospheric Research Centre, State Meteorological Agency of Spain (AEMet), Santa Cruz de Tenerife, Spain, [6]School of Earth, Atmospheric and Life Sciences, University of Wollongong, Wollongong, Australia, [7]Centro de Ciencias de la Atmósfera, Universidad Nacional Autónoma de México, Mexico City, Mexico, [8]Laboratoire d'Etudes du Rayonnement et de la Matière en Astrophysique et Atmosphères, Sorbonne Université, CNRS, Observatoire de Paris, PSL Université, Paris, France, [9]School of Physics, University of Wollongong, Wollongong, Australia, [10]Institute of Astrophysics and Geophysics, University of Liège, Liège, Belgium, [11]Saint Petersburg State University, Saint Petersburg, Russia, [12]Royal Belgian Institute for Space Aeronomy, Brussels, Belgium, [13]National Institute for Environmental Studies, Tsukuba, Japan, [14]Graduate School of Environmental Studies, Tohoku University, Sendai, Japan, [15]Institute for Space-Earth Environmental Research (ISEE), Nagoya University, Nagoya, Japan, [16]University of Bremen, Bremen, Germany, [17]Karlsruhe Institute of Technology, IMK-IFU, Garmisch-Partenkirchen, Germany, [18]National Institute for Water and Air, Lauder, New Zealand

**Special Section:**

Long-term Changes and Trends in the Middle and Upper Atmosphere

**Key Points:**

- Global distribution of carbonyl sulfide (OCS) measured by NDACC solar absorption FTIR remote sensing
- Tropospheric trends in OCS are non-monotonic globally, driven by anthropogenic emissions
- Longest term stratospheric trends are increasing outside of sub-tropics

**Correspondence to:**

J. W. Hannigan,
jamesw@ucar.edu

**Citation:**

Hannigan, J. W., Ortega, I., Shams, S. B., Blumenstock, T., Campbell, J. E., Conway, S., et al. (2022). Global atmospheric OCS trend analysis from 22 NDACC stations. *Journal of Geophysical Research: Atmospheres*, *127*, e2021JD035764. https://doi.org/10.1029/2021JD035764

Received 30 AUG 2021
Accepted 15 JAN 2022

**Author Contributions:**

**Conceptualization:** James W. Hannigan
**Data curation:** Ivan Ortega, Thomas Blumenstock, John Elliott Campbell, Stephanie Conway, Victoria Flood, Omaira Garcia, David Griffith, Michel Grutter, Frank Hase, Pascal Jeseck, Nicholas Jones, Emmanuel Mahieu, Maria Makarova, Martine Mazière, Isamu Morino, Isao Murata, Toomo Nagahama, Hideaki Nakijima, Justus Notholt, Mathias Palm, Anatoliy Poberovskii, Markus Rettinger, John Robinson, Amelie N. Röhling, Matthias Schneider, Christian Servais, Dan Smale, Wolfgang Stremme, Kimberly Strong, Ralf Sussmann, Yao Te, Corinne Vigouroux, Tyler Wizenberg
**Formal analysis:** Ivan Ortega, Shima Bahramvash Shams
**Funding acquisition:** James W. Hannigan
**Methodology:** James W. Hannigan, Ivan Ortega, Shima Bahramvash Shams

## Abstract

Carbonyl sulfide (OCS) is a non-hygroscopic trace species in the free troposphere and a large sulfur reservoir maintained by both direct oceanic, geologic, biogenic, and anthropogenic emissions and the oxidation of other sulfur-containing source species. It is the largest source of sulfur transported to the stratosphere during volcanically quiescent periods. Data from 22 ground-based globally dispersed stations are used to derive trends in total and partial column OCS. Middle infrared spectral data are recorded by solar-viewing Fourier transform interferometers that are operated as part of the Network for the Detection of Atmospheric Composition Change between 1986 and 2020. Vertical information in the retrieved profiles provides analysis of discreet altitudinal regions. Trends are found to have well-defined inflection points. In two linear trend time periods ~2002 to 2008 and ~2008 to 2016 tropospheric trends range from ~0.0 to (1.55 ± 0.30%/yr) in contrast to the prior period where all tropospheric trends are negative. Regression analyses show strongest correlation in the free troposphere with anthropogenic emissions. Stratospheric trends in the period ~2008 to 2016 are positive up to (1.93 ± 0.26%/yr) except notably low latitude stations that have negative stratospheric trends. Since ~2016, all stations show a free tropospheric decrease to 2020. Stratospheric OCS is regressed with simultaneously measured $N_2O$ to derive a trend accounting for dynamical variability. Stratospheric lifetimes are derived and range from (54.1 ± 9.7)yr in the sub-tropics to (103.4 ± 18.3)yr in Antarctica. These unique long-term measurements provide new and critical constraints on the global OCS budget.

## Plain Language Summary

Carbonyl sulfide (OCS) is the most abundant sulfur containing gas in the atmosphere. There are many sources and sinks of OCS and other sulfur species in the atmosphere but most other short lived sulfur species eventually are converted to OCS. It is important to quantify and understand OCS as it can be used to understand $CO_2$ and the carbon cycle and also since it eventually is transported into the stratosphere where it maintains the sulfate aerosol layer at about 20 km into the atmosphere. This layer is very important for earth's energy balance and climate change. In contrast with earlier and less comprehensive reports, this global study from 22 observation stations worldwide, shows stratospheric OCS to be increasing

**Project Administration:** James W. Hannigan
**Resources:** John Elliott Campbell
**Software:** Ivan Ortega, Shima Bahramvash Shams
**Supervision:** James W. Hannigan
**Validation:** James W. Hannigan
**Writing – original draft:** James W. Hannigan, Shima Bahramvash Shams
**Writing – review & editing:** James W. Hannigan, Ivan Ortega, Thomas Blumenstock, Omaira Garcia, Michel Grutter, Frank Hase, Nicholas Jones, Emmanuel Mahieu, Maria Makarova, Martine Mazière, Anatoliy Poberovskii, Dan Smale, Wolfgang Stremme, Kimberly Strong, Ralf Sussmann, Corinne Vigouroux, Tyler Wizenberg

north and south of the equator but decreasing near the equator and to be increasing in the troposphere to 2016 and decreasing since. The main drivers of OCS in the troposphere are the cumulative anthropogenic sources.

## 1. Introduction

Carbonyl sulfide (OCS) is the most abundant sulfur-containing compound in the atmosphere. The near-surface concentration is variable across much of the globe due to a diverse range of sources and sinks. It is chemically stable in the middle troposphere and a culminating reservoir for other abundant biogenic, anthropogenic, and oceanic source species including di-methyl sulfide (DMS) and carbon disulfide ($CS_2$) see, for example, Kettle et al. (2002) and Ma et al. (2020). Consequently it is the largest persistent source of sulfur into the stratosphere (Sheng et al., 2015; Thomason & Peter, 2006) and a key contributor to the stability of the Junge sulfate aerosol layer in the lower stratosphere (Crutzen, 1976; Kremser et al., 2016; Notholt et al., 2006; Turco et al., 1980). Furthermore, OCS has both a direct and indirect effect on the Earth's radiation budget as a maintainer of the aerosol layer and a direct absorber of middle infrared radiation (Brühl et al., 2012; Crutzen, 1976; Turco et al., 1980).

The sources and sinks of OCS and OCS precursors are varied and complex (Campbell et al., 2015; Kettle et al., 2002; Lee & Brimblecombe, 2016; Suntharalingam et al., 2008; Zumkehr et al., 2018). The contribution of direct anthropogenic sources has been recently investigated (Campbell et al., 2015; Lee & Brimblecombe, 2016; Zumkehr et al., 2018). Both direct and indirect anthropogenic bottom up source inventories including rayon production, aluminum manufacture, coal burning, agriculture, pulp and paper manufacture, automobile tires, and burning of biomass fuels (Campbell et al., 2015; Zumkehr et al., 2018) continue to be improved. Their emissions estimates are found to be non-monotonic in the time period studied (1980–2012), increasing in the most recent years, yet continues to maintain large uncertainties. Biomass burning is a direct uncertain but not insignificant source of OCS (Brühl et al., 2012; Notholt et al., 2003; Stinecipher et al., 2019). The extent of biogenic uptake that has a large effect on annual cycles and possibly on long-term trends, given changing climate and biogenic response, especially in the Northern Hemisphere (NH; Montzka et al., 2007), has also been elusive to define with certainty (Friedlingstein et al., 2014; Suntharalingam et al., 2008; Wang et al., 2016; Whelan et al., 2018).

OCS has become an important proxy measurement for understanding $CO_2$ uptake by plants (Campbell et al., 2017). A thorough review of the global OCS budget with a focus on interactions with the biosphere has been undertaken by Whelan et al. (2018). There it is pointed out that to better enable the use of OCS on a large scale for $CO_2$ uptake or gross primary production (GPP) the proxy OCS budget needs to be improved, as the uncertainties in many sources and sinks limit its use. FTIR measurements of both OCS and $CO_2$ were employed in Wang et al. (2016) to observe seasonal cycles of both. Whelan et al. (2018) and Wang et al. (2016) both conclude that top down budgets point to missing source(s). Furthermore, Hilton et al. (2017) in evaluating GPP related drawdown in North America using NOAA aircraft OCS measurements, differentiate plant fluxes from soil fluxes which can vary widely, the latter approaching 30% of the former in some circumstances, and implying the need for continued investigation.

The lifetime of tropospheric OCS is estimated at 2−3yr (Montzka et al., 2007). The persistent tropospheric concentration leads to a constant flux of OCS to the stratosphere (Crutzen, 1976; Kremser et al., 2015; Turco et al., 1980). There are no long-term direct sampling measurements of stratospheric OCS. OCS is a strong spectral absorber at 2,030–2,070 $cm^{-1}$ in the mid-infrared (MIR) and has been measured by remote sensing techniques from different platforms. Early latitudinal FTIR observations of stratospheric OCS from aircraft flying at 12 km were made in 1978 by Mankin et al. (1979). In 2010, Coffey and Hannigan (2010) combined those with later aircraft measurements using the same instrument across a latitude range of 30°–60°N and spanning 1978–2005 yr to determine a positive but not significant trend of $(0.77 \pm 0.80)$%/yr.

A review of MIR spectral observations from ground-based, aircraft, balloon and Atmospheric Chemistry Experiment-Fourier Transform Spectrometer (ACE-FTS) satellite as well as new measurements from the Paris station and the Spectromètre Infrarouge d'Absorption à Lasers Embarqués (SPIRALE) balloon-borne instrument are described in Krysztofiak et al. (2015). With the wide range of latitude with these measurements they are able to show stronger seasonal amplitude of OCS in the total column and stratosphere with increasing latitude. The SPIRALE instrument also measured $N_2O$ and they calculate stratospheric lifetimes of $(68 \pm 20)$ and $(58 \pm 14)$ years at 67°N and 5°S, respectively. Due to the finite time span of the observations no trends are reported. More recently, Toon et al. (2018) used the 30 yr (1989–2016) balloon-borne and ground-based MKIV FTIR dataset observed from various locations ranging from 34° to 68°N and determine no significant trend in stratospheric OCS over that time period. This conclusion is similar to earlier reporting from aircraft measurements (Coffey & Hannigan, 2010) that spans a similar northern mid-latitude range.

Trends in OCS were deduced from the long-term ground based NDACC station at Kitt Peak (32°N) but not included in this work as the total column dataset ends in 2006. The initial work of Rinsland et al. (2002) is updated to the complete Kitt Peak observation record in Rinsland et al. (2008). The initial work focused on the middle tropospheric partial column excluding the tropopause region from 1978 to 2002 and showed a decreasing significant linear trend of (−0.25 ± 0.04)%/yr, 1σ. Updated trends to 2005 and using updated spectroscopic line parameters reduced the downward trend to (−0.100 5 ± 0.0028)%/yr. Rinsland et al. (2008, Figure 4) also reveal a sharp increase in number of observations after 1998 and a qualitative increase during that short time period between the two analyses ~2002 to 2006 that was not addressed at that time. Stratospheric observations from the 1985 ATMOS mission (ATMOS Spacelab3; Zander et al., 1988), 1994 (ATLAS 3; Gunson et al., 1996), and early ACE-FTS to 2008 (Barkley et al., 2008) measurements also showed no statistically significant increase in northern mid-latitude lower stratospheric OCS during that time (Rinsland et al., 2008), a similar finding as Toon et al. (2018) and Coffey and Hannigan (2010).

Most recently, ground-based measurements of OCS were analyzed for the Jungfraujoch station (Lejeune et al., 2016) and three stations in the southern hemisphere (Kremser et al., 2015) building on ground-based retrievals similar to Rinsland et al. (2002). Lejeune et al. (2016) specifically, explores and details the current retrieval for high resolution ground-based spectra. Both studies reveal generally upward trends in total and partial columns that have fairly well defined changes in trends. In particular Kremser et al. (2015) showed overall trends in total column OCS from 2001 to 2015 of (0.73 ± 0.03)%/yr at Wollongong, (0.43 ± 0.02)%/yr at Lauder, and (0.45 ± 0.05)%/yr at Arrival Heights. Although the time-series for each site showed a constant or decreasing burden between the years 2008 and 2012 depending on the station. A similar step in the trends was seen in the free tropospheric (FT) and stratospheric partial columns presented in that work. In Lejeune et al. (2016), they describe three distinct periods of stable trends for the total column at the northern mid-latitude Jungfraujoch station, decreasing during 1995–2002 by (−0.62 ± 0.08)%/yr, then increasing during 2002–2008 to (1.21 ± 0.10)%/yr, and finally a lessening of the upward trend during 2008–2015 to (0.23 ± 0.10)%/yr.

This work expands on the efforts of Kremser et al. (2015) and Lejeune et al. (2016) to characterize long-term trends of OCS in the lower and free troposphere and stratosphere globally. Datasets from 22 globally dispersed sites have been combined to yield a composite view of OCS from 80°S to 80°N. Measurements have been made with NDACC standard instruments. Retrievals have been processed with all critical parameters pre-defined and employed by all research teams to provide a homogeneous final data product per NDACC standards. Trend analyses are performed by one group. The results are a single trend analysis of a harmonized global data series from a dispersed network of cooperating observation stations. Section 2 describes the stations and data collection and data processing. Section 3 describes the analysis of the time series, regression analyses, annual cycles, latitudinal distributions, stratospheric lifetimes, and discussion from the global perspective. Section 4 present the conclusions.

## 2. Stations and Observations

The data presented here leverage the organization of the NDACC (www.ndacc.org; Kurylo & Soloman, 1990) to produce high-quality consistent long-term datasets from globally distributed stations. An current overview of the NDACC can be found in De Mazière et al. (2018) published in Atmospheric Chemistry and Physics, in a joint special issue with Atmospheric Measurement Techniques and Earth System Science Data. Furthermore, information on the Infrared Working Group (IRWG) can be found at www2.acom.ucar.edu/irwg including lists of species data that are part of the standard IRWG data products. Data used for this analysis are available at www.ndacc.org and by request from the station PI.

### 2.1. Stations

There are 21 globally dispersed NDACC FTIR observation stations that comprise the IRWG, these are listed in Table 1. The station at CNRS, Paris (PRS) is not yet currently part of the IRWG though they make measurements in accordance with IRWG standards is included in Table 1. The map in Figure 1 shows the locations of the

**Table 1**
*Stations Contributing to Carbonyl Sulfide Analysis*

| Station | Location | North latitude | East longitude | m.a.s.l. | Managing institution |
|---|---|---|---|---|---|
| EUR | Eureka | 80.05 | 273.58 | 610 | University of Toronto |
| NYA | Ny Ålesund | 78.90 | 11.90 | 20 | University of Bremen |
| TAB | Thule | 76.53 | 291.26 | 225 | NCAR |
| KIR | Kiruna | 67.84 | 20.41 | 420 | KIT-ASF |
| STP | St Petersburg | 59.88 | 29.83 | 20 | University of Saint Petersburg |
| BRE | Bremen | 53.10 | 8.90 | 27 | University of Bremen |
| PRS | Paris | 48.85 | 2.36 | 60 | LERMA |
| ZUG | Zugspitze | 47.42 | 10.98 | 2,964 | KIT-IFU |
| JFJ | Jungfraujoch | 46.55 | 7.98 | 3,580 | University of Liège |
| TOR | Toronto | 43.66 | 280.60 | 174 | University of Toronto |
| RKB | Rikubetsu | 43.46 | 143.77 | 380 | University of Nagoya |
| BLD | Boulder | 40.04 | 254.76 | 1,612 | NCAR |
| TSK | Tsukuba | 36.05 | 140.12 | 31 | NIES |
| IZA | Izaña | 28.30 | 343.52 | 2,370 | KIT-ASF |
| MLO | Mauna Loa | 19.54 | 204.43 | 3,396 | NCAR |
| ALZ | Altzomoni | 19.12 | 261.35 | 4,010 | UNAM |
| PMB | Paramaribo | 5.81 | 304.79 | 7 | University of Bremen |
| MAI | Reunion Island Maïdo | −21.07 | 55.38 | 2,160 | BIRA |
| STD | Reunion Island Saint Denis | −21.09 | 55.48 | 50 | BIRA |
| WLG | Wollongong | −34.41 | 150.88 | 30 | University of Wollongong |
| LDR | Lauder | −45.05 | 169.67 | 370 | NIWA |
| AHS | Arrival Heights | −78.83 | 166.66 | 200 | NIWA |

*Note*. Station abbreviation, station location name, location coordinates, and managing institution.

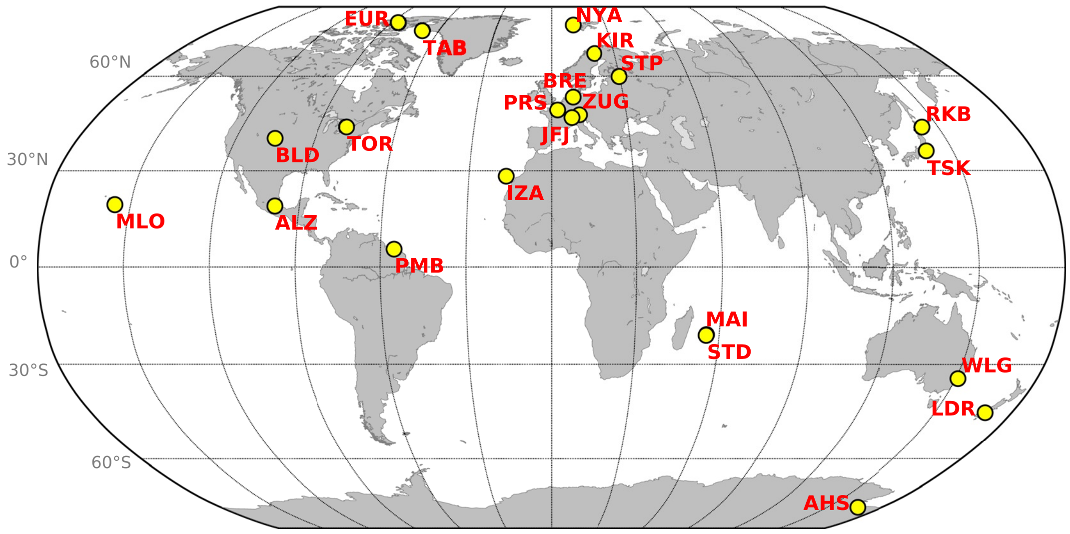

**Figure 1.** Global map of NDACC FTIR stations contributing to this study. *Note*. PRS is not yet currently a formal NDACC station.

**Table 2**
*Spectral Regions, OCS Absorption Features, and Possible Interfering Species Used for the Optimal Estimation Retrieval of OCS*

| Microwindow [$cm^{-1}$] | OCS absorption line | Interfering species |
|---|---|---|
| (1) 2,030.75–2,031.06 (optional) | – | $CO_2$, $O_3$ |
| (2) 2,047.85–2,048.24 | P(32) | OCS, $CO_2$, $O_3$ |
| (3) 2,049.77–2,050.18 | P(28) | OCS, $H_2O$, $^{12}C^{16}O^{18}O$, $O_3$, CO |
| (4) 2,054.33–2,054.67 | P(18) | OCS, $H_2O$, $H_2^{18}O$, $CO_2$, $O_3$ |

*Note*. OCS, carbonyl sulfide.

contributing stations. Observations from all sites continue to the present. Initial operations and consequent data record duration vary by station from Jungfraujoch in 1986 to Altzomoni in 2012.

Solar-viewing FTIR spectra are acquired in accordance with standards set forth by the IRWG (www.acom.ucar.edu/irwg/links). These are high spectral resolution (minimum OPD = 180 cm, 250 cm typical), instruments that can record spectra in selected spectral bandpass regions through the mid-infrared (MIR) from 750 to 5,000 $cm^{-1}$ and instruments that can record a single interferogram in under 1 min. Observations are made routinely, often multiple times per day weather permitting. Several early ground-based OCS studies were performed (Mahieu et al., 1997; Jungfraujoch) (Griffith et al., 1998; Wollongong and Lauder), and (Rinsland et al., 2002, 2008; Kitt Peak). More recently an analysis of southern hemisphere OCS was revisited by Kremser et al. (2015) using data from the NDACC stations at Wollongong, Lauder and Arrival Heights. A thorough review of details and parameters to maximize information content and optimize profile retrieval from ground-based spectra was performed by Lejeune et al. (2016) using spectra from the Jungfraujoch.

## 2.2. Observations and Retrievals

The retrieval strategy adopted here is largely based on the optimized spectral regions and spectroscopy reported by Lejeune et al. (2016). Table 2 shows the micro-windows and species with absorption features that may affect the total spectral absorption. Three features of the $\nu_3$ fundamental of OCS are fitted in the retrieval. The region at 2,030 $cm^{-1}$ is employed at some stations to improve the characterization of the interfering species of $CO_2$ and $O_3$. The spectroscopic parameters are based on HITRAN 2012 (Rothman et al., 2013). The ATM16 line parameter list (Geoff Toon, JPL, PC) was also tested to assess the linelist impact on OCS but for these OCS spectral regions did not result in an improvement in fit quality, interference from other species, or retrieved column. These three OCS absorption features are stable and have not been improved in later HITRAN releases 2016 and 2020. To reduce the effects of water vapor it is typically pre-retrieved before each OCS retrieval such that it is more accurate as a priori in the OCS retrieval.

The retrieval analysis for the ground-based FTIR spectra uses a form of the optimal estimation (OE) technique Rodgers (1976, 1990, 1998, 2000). There are two-independent operational code sets that are used exclusively within the IRWG: these are PROFFIT (Hase et al., 2004) and SFIT (Pougatchev et al., 1995; Rinsland et al., 1998; https://wiki.ucar.edu/display/sfit4/). They have been previously thoroughly inter-compared (Hase et al., 2004) and have been the algorithms used in many NDACC-wide trace gas trend analyses and validation efforts, for example, Buchholz et al. (2017), Dammers et al. (2017), Gaudel et al. (2018), Kohlhepp et al. (2012), Olsen et al. (2017), and Vigouroux et al. (2015). The forward model and state vector rely on a priori data. Retrieval accuracy and precision are improved with a priori data as close to the observed state as possible (Pougatchev et al., 1995) and with statistically coherent associated uncertainties i.e. covariances (Rodgers, 2000).

Furthermore, for a globally distributed set of independent measurements as are employed here, internally consistent a priori data are needed. Much of this is incorporated in operational NDACC standards (www.acom.ucar.edu/irwg/links). The retrieval grid is common for all sites at altitudes above ~7 km and adjusted consistently below ~7 km to accommodate the local observation altitude. Initial pressure and temperature profiles are NCEP analyses provided at (www.ndacc.org; Finger et al., 1993; Wild et al., 1995). For chemical a priori profiles of interfering species noted in Table 2, modeled climatological means are used.

**Table 3**

*Number of Profiles Used From Each HIPPO and ACE-FTS Dataset by Latitude Bin Required for A Priori Consistency*

| Latitude bin | HIPPO surface 14 km | ACE-FTS 14–30 km |
|---|---|---|
| 50.0 to 90.0 | 17 | 12,577 |
| 20.0 to 50.0 | 12 | 2,830 |
| −20.0 to 20.0 | 11 | 1,957 |
| −50.0 to −20.0 | 11 | 2,536 |
| −90.0 to −50.0 | 5 | 12,125 |

*Note*. HiPPO, Hiaper pole-to-pole observations.

Chemical profiles for all targeted NDACC and many background species have been generated from Whole-Atmosphere Community Climate Model, Version 4 (WACCM4) for all NDACC IRWG, NDACC LIDAR, and many other stations for use as retrieval priors. This includes the interfering species noted in Table 2 and $N_2O$ used in Section 3.4 These a priori profiles have several advantages over other sources of a priori information. The modeled data employs surface emission data that can provide more accurate low altitude mixing ratios that the FTIR retrieval may not be sensitive to and may not be included in other a priori sources, for example, satellite profiles. The derived mean a priori from a long-term model run also yields a measure of variability that can be used as the covariance for retrievals and for understanding smoothing by the retrieval. To the accuracy of the model, the interspecies correlations are self-consistent. The global surface to mesosphere model provides consistency for all sites in the altitude range of interest, and sensitivity of the FTIR retrievals. There is no observational dataset with this complete self-consistency for more then 60 trace species otherwise available for this purpose, consequently, the IRWG adopted a run of the WACCM4 model (Garcia et al., 2007) for priors for retrieved species and for profiles for background or interfering species. To provide a priori that are minimally biased over the long-term, the a priori are computed as an average from monthly sampling of the 40 yr portion from 1980 to 2020 of a 75 yr Stratosphere-troposphere Processes And their Role in Climate (SPARC) Chemistry Climate Model Initiative (CCMI) model inter-comparison. The CCMI validation was a continuation of the CCMVal project as described in Eyring et al. (2007) and compares several models under specific Intergovernmental Panel on Climate Change (IPCC) scenarios for $O_3$ recovery. In particular we use a moderate set of scenarios following REFC1.3 and IPCC scenarios A1B for greenhouse gases emissions, AR4 for sea surface temperatures and surface Halogen Ab prescribed by WMO/UNEP. Details can be found in Eyring et al. (2007). These a priori chemical profiles, interpolated to station location and altitude, provide a reasonable mean from which observations will vary. The a priori profiles were tested for applicability at all sites before adoption as an NDACC a priori standard. These data are used for the a priori of the interfering species given in Table 2.

Unfortunately profiles for OCS are not included in the large suite of WACCM4 species (we expect these will be part of the forthcoming version). In order to attain a globally consistent a priori dataset that also spans the net OCS seasonal cycle, datasets from the National Science Foundation (NSF), High-performance Instrumented Airborne Platform for Environmental Research (HIAPER), airborne campaign Pole-to-Pole Observations (HIPPO; www.eol.ucar.edu/field_projects/hippo), and satellite-borne ACE-FTS (www.ace.uwaterloo.ca/instruments_acefts.php; Boone et al., 2013) were used. The tropospheric dataset, used for the profile component below 14 km, is comprised of the accumulated datasets from HIPPO missions 1 through 5, spanning a latitude range of 85°N–67°S reaching all FTIR stations but Arrival Heights sampling different seasons over a 2.4 yr operational window during 2009–2011 (Wofsy, 2011; Wofsy et al., 2017). The stratospheric portion of OCS is obtained from ACE-FTS v3.5 between 2004 and 2013 (Boone et al., 2013; Velazco et al., 2011). From these data, mean profiles and covariances were derived. To account for latitudinal variability without over-burdening the somewhat sparse HIPPO dataset composite profiles were binned into five zonal regimes: 90°−50°N, 50°−20°N, 20°N−20°S, 20°–50°S, and 50°–90°S. Table 3 lists the number of raw profiles available for reduction to zonal a priori. The profiles were interpolated to a 1 km grid, averaged for each latitude bin and concatenated at 14 km. The ACE-FTS derived zonal profiles were found to be biased low by ∼15% relative to the HIPPO datasets at 14 km. A similar negative bias for the ACE-FTS OCS has also been reported previously with respect to the MK-IV FTS (Velazco et al., 2011), MIPAS (Glatthor et al., 2017), and SPIRALE (Krysztofiak et al., 2015). Consequently for purposes here, a positive shift of ∼15% is applied to the ACE-FTS profiles to match the upper tropospheric portion of the HIPPO in situ profiles. Above the ACE-FTS max altitude, the profiles were tapered to 0.015 pptv (parts per trillion by volume) at 50 km and above with no consequence to this analysis, due to the rapidly diminishing sensitivity above 30 km altitude. The profiles were smoothed by a Savitsky-Golay function with a 9 km window width and polynomial of order 3. The left panel of Figure 2 show the final concatenated and smoothed a priori vertical profiles binned to latitudinal zones. The right panel Figure 2 are one $\sigma$ ($\sigma$ will be used consistently to note 1 standard deviation of the population being discussed) curves derived from all contributing profiles. These curves are then used as initial diagonal components of the a priori state vector covariances ($S_a$) in the OE retrieval scheme.

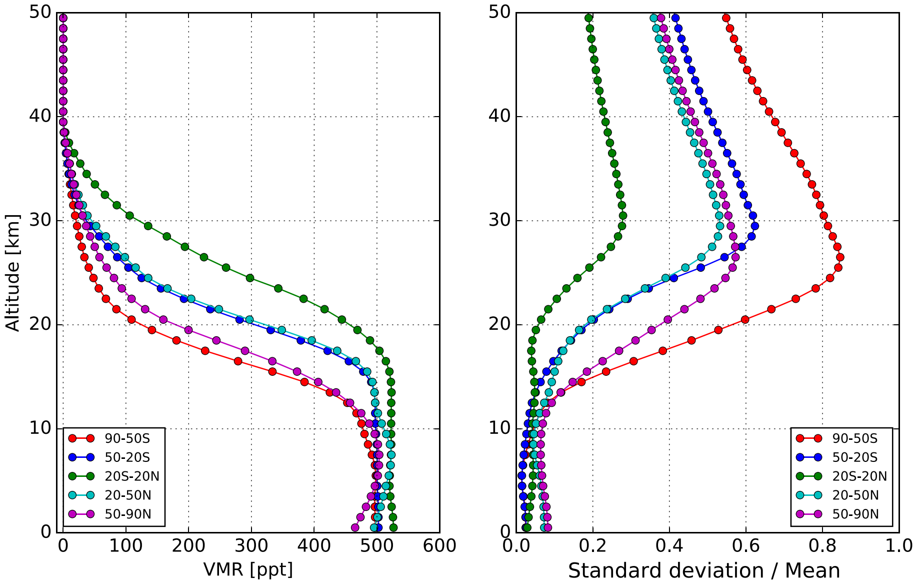

**Figure 2.** A priori vertical profiles of OCS binned by latitudes as in Table 3 derived from concatenated and smoothed global HIPPO and ACE-FTS data. In the left panel are the observation based a priori profiles as described in the text. In the right panel are the standard deviation from all profiles for that bin used for the $S_a$ covariance (see text for details).

To create the OCS retrieval $S_a$ matrix the diagonal elements are interpolated and normalized to the variable layer thickness retrieval grid by the square root of the thickness. Finally the off-diagonal elements of the $S_a$ matrix are calculated using a Gaussian function with a 4 km half width that aids in maximizing information content.

The profile retrievals are shown in Figure 3. Figure 3 (and several similar to follow) show results for each station with panels displayed from high to low latitude from top to bottom. The background color shading illustrates the five latitude zones given in Table 3. The vertical response of the retrieval is characterized in the averaging kernels (AK) and by the accumulated scalar degrees of freedom for signal (DOFS; Rodgers, 1998, 2000). These are shown for all sites in Figure 4. For each site, the left panel are the common retrieval grid volume mixing ratio (VMR) averaging kernels. These show the typical broad kernels that are indicative of the limited vertical resolution of the retrieval system. Yet, they also reveal peaks in the troposphere and lower stratosphere that we exploit in the multi-layer analysis. The middle panels are the total column averaging kernel indicating the altitude sensitivity of the integrated total column amount. The right panels are the accumulated DOFS summed from the observation altitude upwards, where DOFS values vary over a small range from ~2.5 at lower latitudes to ~3 at higher latitudes but will also depend on station altitude and the instrument signal-to-noise (SNR).

### 2.2.1. Uncertainties and Information Content

An uncertainty analysis for the state vector for all species retrieved within the guidance of the NDACC IRWG follow the formalism of the OE technique (Rodgers, 1990). The uncertainty calculations are part of the standard IRWG retrieval processing to maintain homogeneity across the network and species and is discussed in a number of publications, for example, Lejeune et al. (2016) and Vigouroux et al. (2008, 2018). This reveals the quantitative contribution of the principle components of the observation and retrieval system to the uncertainty in the state vector and in particular the retrieved VMR profiles. Given the homogeneity of the observing systems from instrumentation through retrieval, we detail here, representative uncertainty budgets for three stations: TAB, BLD, and MLO. They represent a range of observation characteristics that can effect a ground-based retrieval and its associated uncertainty. These stations span a range of latitudes: 20°, 40°, and 76°N, of observation altitudes: 0.22, 1.6, and 3.45 km a.s.l., proximity to anthropogenic or biogenic sources from remote Arctic to continental suburban mid-latitude to sub-tropic Pacific island. Uncertainty profiles for principle uncertainty components are calculated at each altitude layer for each retrieval. Uncertainty profiles for random and systematic components for a single retrieval from each site are plotted in Figure 5 in percent of the a priori VMR profile.

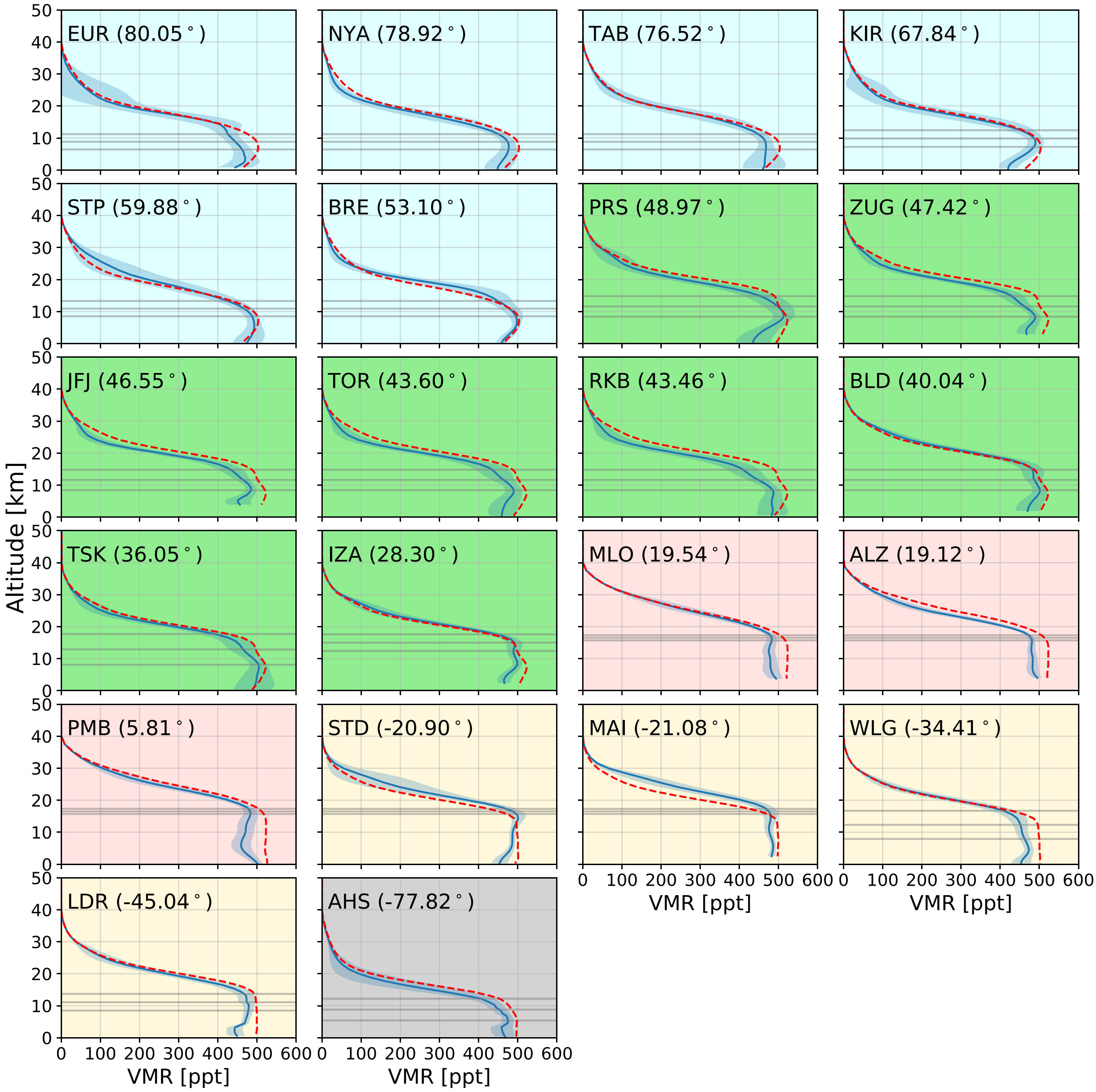

**Figure 3.** Mean OCS vertical profiles at all sites (blue continuous lines). The blue shaded area represents the standard deviation of all retrievals. Red dashed lines are the a priori from HIPPO + ACE-FTS data, see Figure 2. The mean tropopause height and 2× standard deviation as defined in the text are shown in horizontal grey lines. At the top of each plot is the station ID and latitude. Panels are color coded to the a priori bins given in Table 3, the same convention will be repeated in subsequent plots.

Random components are the measurement, interfering species, temperature profile variability, solar zenith angle, and background retrieval parameters. Of these all remain below 2% of the VMR profile for all altitudes except the measurement error which peaks in the stratosphere between 25 and 28 km and varies in magnitude with station at 15%, 10%, and 6% at TAB, BLD, and MLO, respectively. Systematic components are the temperature profile bias, phase function, HITRAN parameters: line intensity ($S$), air broadened half width ($\gamma$), and the coefficient of the temperature dependence of the air-broadened half width ($n$). Of these all contribute less than 3% except the air broadened half width which contributes up to 12% at 13 km at TAB, between 7.5% and 9.5% between 12 and 26 km at BLD and peaking at 26 km at 13% at MLO.

More appropriate for the data presented below, are the random, systematic, and total uncertainties expected for each analysis layer (LT, FT, and LS) for these three sites. Table 4 gives the mean and standard deviation

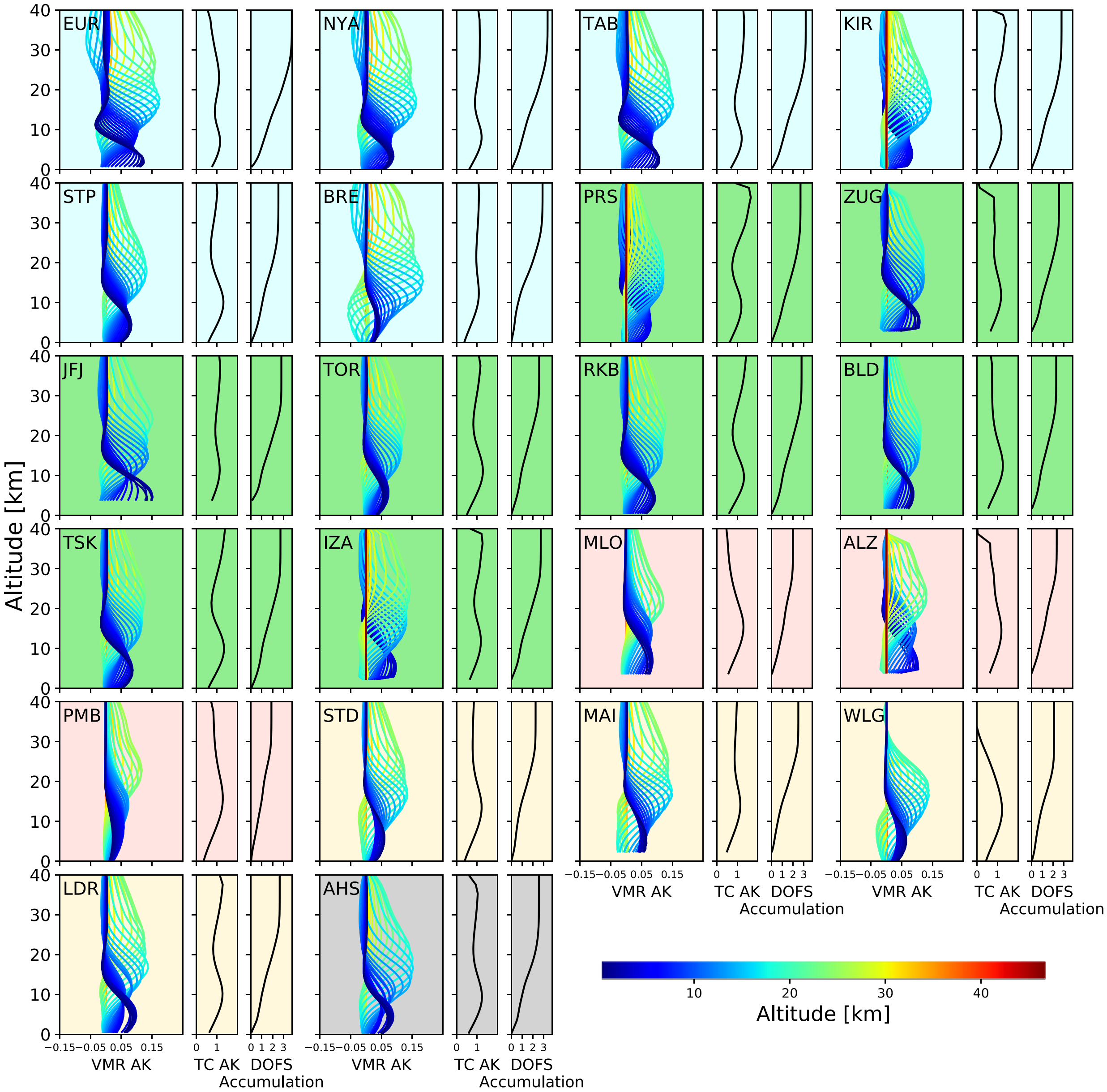

**Figure 4.** Characteristics of the retrieval for each station as a function of altitude. The leftmost plot per site are the averaging kernels on the retrieval grid color coded by altitude. The center plot is the total column averaging kernel and the rightmost plot is the DOFS, accumulated from the observation altitude to top of atmosphere.

uncertainties for a single retrieval in pptv from the average of retrievals in 2019. The low standard deviations illustrate the consistency of the typical data discussed here. The rightmost column are the accumulated DOFS in that layer for that site and as noted can vary with station latitude and observation altitude. The total DOFS increase from 2.0 to 3.3 with increasing latitude as do the stratospheric partial columns from 0.9 at MLO to 1.9 at TAB. The FT DOFS primarily reflect the tropopause height and decrease with latitude with a minimum of 0.6 at TAB. This is slightly lower than the low troposphere at TAB of 0.7. We expect all stations to follow similar patterns and quantitatively similar DOFS. The lowest value is seen at BLD with an observation altitude of 1.6 km and a LT upper limit at 4 km. Other stations that would also have low tropospheric DOFS are Maïdo at 2,160 m.a.s.l. and Izãna at 2,370 m.a.s.l. Stations nearer sea level will typically have larger overall DOFS. Although these few stations with low DOFS have lower information we keep the data series to complete the analysis and note the data may include more information from the a priori than the others.

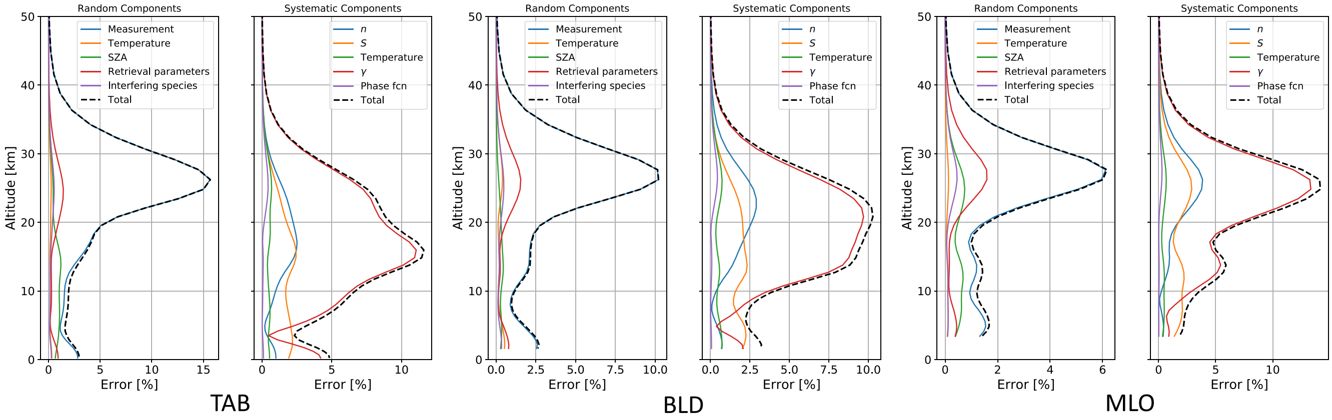

**Figure 5.** Uncertainty profiles for three latitudinally dispersed stations: Thule, Greenland, Boulder, CO, USA, and Mauna Loa, HI, USA (left, center, and right, respectively). For each site, the left panel are random components and total and the right panel are systematic components and total. These profiles for a single retrieval of ∼2 min measurement integration time and are given in percent of the a priori profile. Components are described in the text but in particular systematic components: $\gamma$ is the Lorentzian air broadening half width, $n$ is the exponent of the dependence of the air broadening half width, and $S$ is the line intensity.

Regarding layer independence, from Figure 3 it can be seen that the retrievals exhibit slightly lower mixing ratios than the a priori for the tropospheric layers that is not seen systematically in stratospheric retrievals. The actual biases are given in Table 5. Biases range from −0.80 pptv at TSK to −11.92 at PRS in the LT and −1.049 at BRE to −10.21 at PMB in the FT.

## 3. Time Series and Long-Term Trends

The time series data will be represented with monthly means of the total column and partial columns that are given as mean mixing ratios for altitude regimes commensurate with the DOFS of the retrievals and detailed below.

Figure 6 shows the time series of monthly mean total columns for all stations. The monthly means retain the long-term trend information excluding very short-term variability. Column or concentration data for each site is plotted using the same ordinate and abscissa scale to more easily illustrate the global perspective on trends at all sites. Variation in station altitude and latitude are reflected in the total column amounts. All sites show an annual cycle, that is, affected in part by the annual variation of the aggregate of sources and sinks and tropopause height

**Table 4**
*Typical Random, Systematic, and Total Uncertainties for a Single Retrieval by Altitude Layer for Three Latitudinally Dispersed Stations: Thule, Greenland, Boulder, CO, USA, and Mauna Loa, HI, USA*

| Station | Altitude region | Random | Systematic | Total | Mean DOFS |
|---|---|---|---|---|---|
| TAB | Low troposphere | 11.48 ± 1.27 | 17.36 ± 3.44 | 20.99 ± 2.81 | 0.7 |
| | Free troposphere | 8.21 ± 2.15 | 20.97 ± 3.69 | 22.66 ± 4.01 | 0.6 |
| | Stratosphere | 9.72 ± 0.91 | 28.72 ± 2.09 | 30.79 ± 2.00 | 1.9 |
| | Total column [%] | 1.28 ± 0.42 | 2.77 ± 0.32 | 3.08 ± 0.35 | 3.3 |
| BLD | Low troposphere | 12.46 ± 1.48 | 14.86 ± 2.52 | 19.56 ± 1.50 | 0.4 |
| | Free troposphere | 7.03 ± 0.83 | 16.24 ± 1.03 | 17.98 ± 0.83 | 0.8 |
| | Stratosphere | 9.27 ± 0.56 | 31.79 ± 1.66 | 33.50 ± 1.65 | 1.4 |
| | Total column [%] | 1.08 ± 0.21 | 2.84 ± 0.28 | 3.04 ± 0.33 | 2.7 |
| MLO | Free troposphere | 6.84 ± 0.89 | 15.68 ± 1.55 | 17.40 ± 1.63 | 1.0 |
| | Stratosphere | 6.95 ± 0.51 | 26.13 ± 1.57 | 27.14 ± 1.48 | 0.9 |
| | Total column [%] | 1.02 ± 0.22 | 2.90 ± 0.18 | 3.09 ± 0.16 | 2.0 |

*Note*. Values are in pptv for the layers and percent of the mean for the total column. They are average $\pm 1\sigma$ for all retrievals for 2019. The right column is the mean DOFS for the same dataset. DOFS, degrees of freedom for signal.

**Table 5**
*Bias in Percent of the A Priori, of the Mean Retrieved Profile for all Retrievals at Each Site. These Are the Profiles Shown in Figure 2*

| Station | Low troposphere | Free troposphere |
|---|---|---|
| EUR | −3.61 | −8.16 |
| NYA | −4.66 | −5.21 |
| TAB | −2.98 | −6.73 |
| KIR | −10.02 | −4.33 |
| STP | 1.21 | −2.08 |
| BRE | −1.53 | −1.05 |
| PRS | −11.92 | −4.06 |
| ZUG | −8.32 | −7.39 |
| JFJ | – | −8.89 |
| TOR | −7.49 | −6.96 |
| RKB | −3.25 | −7.23 |
| BLD | −5.28 | −6.87 |
| TSK | −0.80 | −3.75 |
| IZA | −8.41 | −4.27 |
| MLO | – | −8.02 |
| ALZ | – | −7.50 |
| PMB | −7.29 | −10.21 |
| STD | −7.17 | −1.41 |
| MAI | −2.90 | −3.04 |
| WLG | −8.06 | −7.32 |
| LDR | −10.57 | −4.92 |
| AHS | −6.83 | −5.12 |

(latitude dependent). The large step in the data for the St Denis-Maïdo (STD-MAI) station which is the concatenation of the Saint Denis station data record (early) and Maïdo record (later data) is due to the altitude change from the Saint Denis site at sea level to Maïdo at 2.16 km.a.s.l.

To analyze the long-term trend and annual cycle and account for unevenly sampled time series when needed, we use a bootstrap re-sampling tool (Gardiner et al., 2008) and Equation 1:

$$f(t) = a_0 + a_1 (t - t_0) + \sum_{n=1}^{N} b_n \cos\left(\frac{n\pi x}{L}\right) + \sum_{n=1}^{N} c_n \sin\left(\frac{n\pi x}{L}\right) \quad (1)$$

where the first two terms correspond to the linear component: $a_0$ is the intercept value, $a_1$ is the long-term trend (or slope) of the observation time $t$, and $t_0$ is the time of the first observation. The second and third terms are the Fourier series to fit the seasonal modulation where $N = 2$. A bootstrap population of 5,000 is used, yielding the mean slope ($a_1$) and distribution half width that are used to quantify the trend and its $1\sigma$ uncertainty. The annual rate of change relative to the mean, calculated with the linear portion of Equation 1, is estimated with the anomalies (FTIR($t$) − $f$($t$)) using the seasonal components of the fit calculated with Equation 1 to account for seasonal variability.

Figure 7 shows the total column anomalies now fitted with a fifth-order polynomial to illustrate slowly varying changes in the trend (blue line). The total column data is generally increasing at all these stations over this time period but not monotonically. The polynomial fit reveals changes from a linear trend. For the longest term sites, these show a minimum in 2001–2002. For most of these another change in slope is at ~2008. Similar inflection points were exhibited in earlier work in the southern (Kremser et al., 2015), and northern (Lejeune et al., 2016) hemispheres and here are shown to be a more universal feature seen in the dataset globally. We will discuss trends

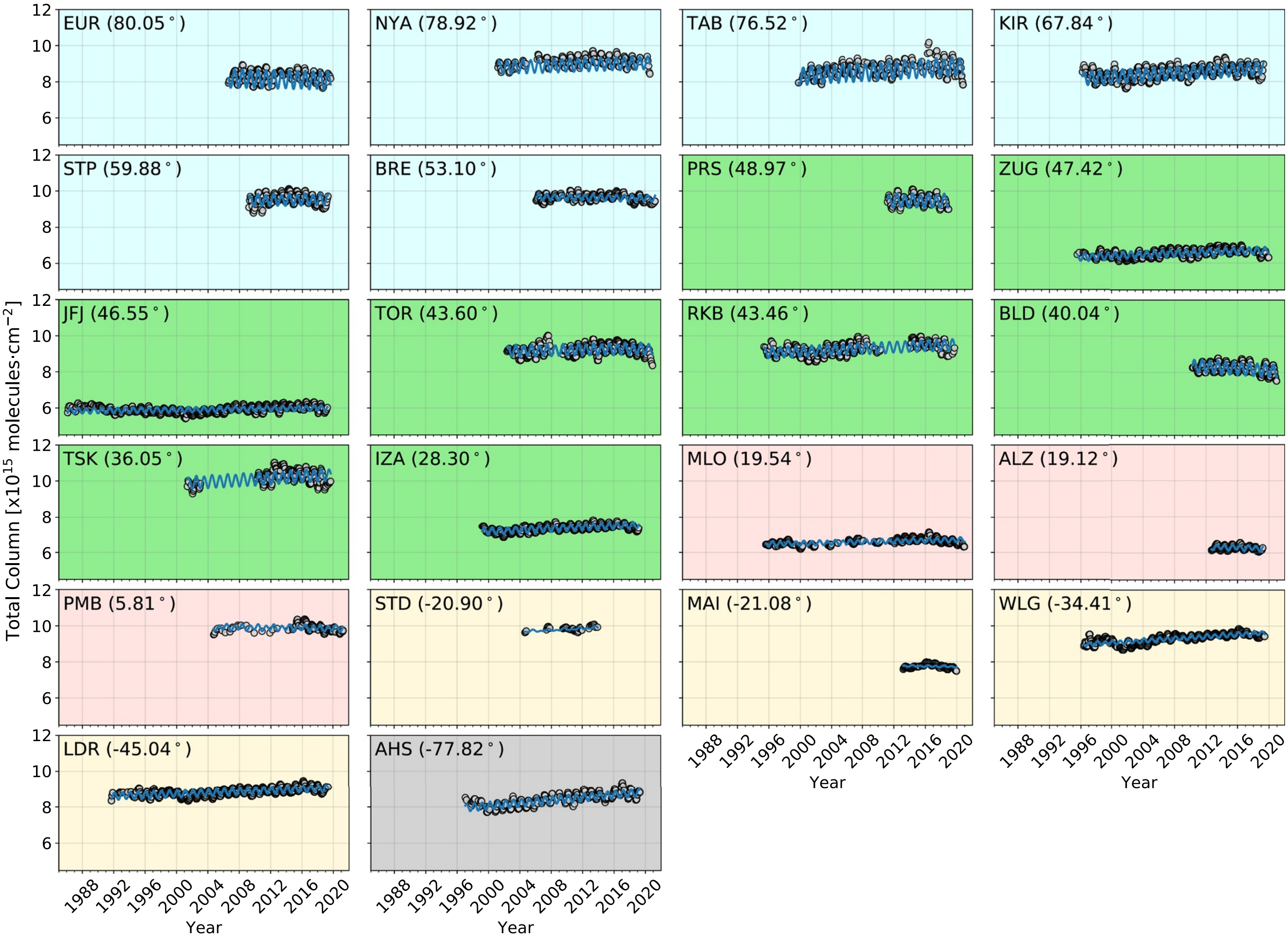

**Figure 6.** Time series of OCS total column for all sites on the same ordinate and abscissa scale. Gray circles represent the monthly mean observational data. The blue line is the seasonal modulation and trend component of the monthly mean total column using Equation 1.

in these time periods below. As mentioned in the Introduction total column from Kitt Peak show a decreasing linear trend from 1978–2002 of (−0.25 ± 0.04%/yr; Rinsland et al., 2002) and of (−0.1005 ± 0.0028%/yr) shown in Rinsland et al. (2008, Figure 4). The later also shows a qualitative leveling during that short time period between 2002 and 2006 that while not addressed at that time is a feature seen at other stations (see below).

The longer Arctic time series (NYA, TAB, and KIR) seem to show a delay in this feature. There is a slow increase to 2006 then a leveling off or decline with a resumed increase nearer 2014. In TAB this is offset by anomalously high values in early 2016. In the SH high values are seen at two stations WLG and AHS in 1996–1999 before rapidly dropping to minima around 2002.

We have obtained data for most stations up through 2019 or 2020. Figure 7 clearly show another likely inflection point other than those described above, in the time series record at the period of ~2016 to 2018 at stations for example, TAB, KIR, TOR, LDR, and AHS. To draw conclusions on the increasing trends in the last decade we calculate a linear trend for the 2008–2016 period as discussed below. The inflection point at ~2016 to 2018 seen in Figure 7 is clear but too recent and too short a time period to draw any conclusion as to the current rate of the decrease.

### 3.1. Tropopause Height and Layer Isolation

The latitudinally dependent annual cycle of the tropopause height (TH) coupled with the OCS vertical profile (see Figure 3) that rapidly decreases above the tropopause imposes a problematic annual signal on the retrieved

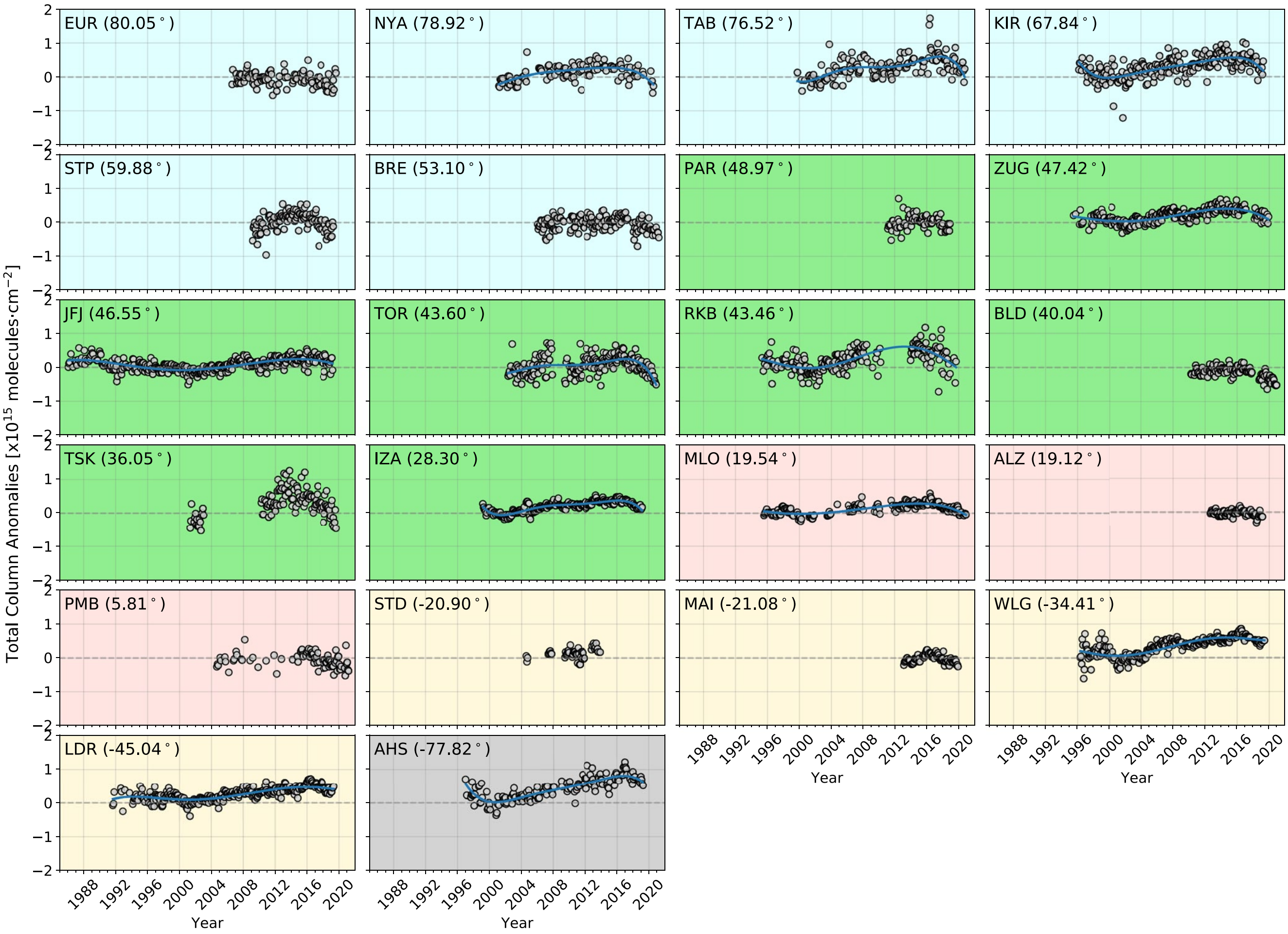

**Figure 7.** Time series of OCS total column anomalies for all sites on the same ordinate and abscissa scale, see text for derivation. Gray circles represent monthly mean observational anomalies. The blue curve is fit to the anomaly with a fifth-order polynomial showing changes in trend to several of the longest time series (NYA, TAB, KIR, ZUG, JFK, TOR, RKB, IZA, MLO, WLG, LDR, and AHS; see Equation 1).

profiles. To make the best use of the limited vertical resolution illustrated in Figure 4, while minimizing the effect of the variable TH, layers relative to the tropopause are defined. Further the mean mixing ratio, that is, independent of the optical path through the the layer is calculated. Table 6 shows the NCEP temperature derived tropopause height for each station. We compared this TH method with the more precise dynamical tropopause height (Zängl & Hoinka, 2001; and M. von Hobe, PC) and found this method adequate for this analysis due to the coarse vertical resolution of the measurements.

Altitude ranges are chosen in an attempt to isolate the free troposphere where OCS dominates the sulfur budget, from large surface sources and sinks regime and the stratosphere while minimizing the effects of annual tropopause height cycles which vary in altitude with latitude to clarify long-term trends distinguishing the source region from the stratosphere. As shown in Figure 4 the OCS retrievals yield sufficient information (DOFS up to ~3) to detail three altitude ranges. These analysis ranges are: observation altitude to 4 km, 4 km to TH $- 2\sigma$, and TH $+ 2\sigma$ to 40 km. The choice of 4 km also keeps the FT region from high altitude sites for example, JFJ, MLO, and ALT on equal footing as other sites see Table 1.

### 3.2. Trends by Layer

On the standardized retrieval grid there is still a small variation in layer thickness nearer the observation altitude for each site. We define a weighted mixing ratio (wVMR) for the three integrated analysis layers calculated with the following expression:

**Table 6**
*Tropopause Height Statistics Determined From NCEP Data for All Observation Days at All Sites Binned in ~10° Zonal Regions Excluding Subtropic and Southern Mid-Latitudes*

| Station | Latitude [°N] | Mean ± SD [km] | Maximum [km] | Minimum [km] | Pk–Pk [km] | Latitude bin |
|---|---|---|---|---|---|---|
| EUR | 80.1 | 8.8 ± 1.1 | 11.2 | 6.2 | 2.0 | 90°–70°N 8.8 ± 1.2<br>Pk–Pk = 2.1 |
| NYA | 78.9 | 8.9 ± 0.9 | 11.3 | 6.7 | 2.2 | |
| TAB | 76.5 | 8.7 ± 1.1 | 11.4 | 5.7 | 2.2 | |
| KIR | 67.8 | 9.8 ± 1.1 | 12.9 | 6.8 | 1.4 | 70-60°N |
| STP | 59.9 | 10.5 ± 1.0 | 12.8 | 7.2 | 1.9 | 60°–50°N 10.9 ± 1.2<br>Pk–Pk = 1.7 |
| BRE | 53.1 | 11.2 ± 0.9 | 14.0 | 8.2 | 1.5 | |
| PRS | 49.0 | 11.7 ± 0.9 | 13.6 | 9.1 | 1.4 | 50°–40°N 11.6 ± 1.4<br>Pk–Pk = 3.0 |
| ZUG | 47.4 | 11.7 ± 1.1 | 15.1 | 8.3 | 2.0 | |
| JFJ | 46.5 | 11.7 ± 1.1 | 15.7 | 8.1 | 2.0 | |
| TOR | 43.6 | 12.0 ± 1.8 | 15.8 | 7.6 | 4.2 | |
| RKB | 43.5 | 10.7 ± 2.0 | 16.5 | 7.4 | 5.4 | |
| BLD | 40.0 | 13.3 ± 1.8 | 16.4 | 9.5 | 4.3 | |
| TSK | 36.0 | 12.6 ± 2.4 | 16.7 | 7.3 | 6.6 | 40°–30°N |
| IAZ | 28.3 | 15.1 ± 1.1 | 17.6 | 11.2 | 2.1 | 30°–20°N |
| MLO | 19.5 | 16.1 ± 0.6 | 17.6 | 11.9 | 0.8 | 20°N–25°S 16.5 ± 0.4<br>Pk–Pk = 0.7 |
| ALZ | 19.1 | 16.5 ± 0.4 | 17.6 | 15.7 | 1.0 | |
| PMB | 5.8 | 16.5 ± 0.2 | 17.2 | 16.0 | 0.5 | |
| STD-MAI | −20.9 | 16.6 ± 0.3 | 17.4 | 15.8 | 0.5 | |
| WLG | −34.4 | 12.3 ± 2.0 | 17.4 | 8.2 | 4.4 | 25°–45°S 11.7 ± 1.6 |
| LDR | −45.0 | 11.1 ± 1.2 | 16.6 | 8.6 | 2.3 | Pk–Pk = 3.3 |
| AHS | −77.8 | 8.8 ± 1.5 | 14.1 | 6.2 | 3.8 | 50°–90°S |

$$wVMR = \frac{\sum_{z=1}^{n} x_z \cdot K_z}{\sum_{z=1}^{n} K_z} \tag{2}$$

where $w$VMR is the final weighted mixing ratio of OCS in that layer, $z$ is the altitude layer on the retrieval grid, $x_z$ is the retrieved mixing ratio in that layer, and $K_z$ is the associated air mass. The $w$VMR is an easily comparable quantity independent of the actual layer thickness which may vary at each site.

Figure 8 shows the anomalies for the lower tropospheric (LT) layer monthly mean mixing ratios, segregated into periods of general linear trend. Observation altitude for stations ALZ, JFJ, and MLO are above this layer. Due to the complex sources and sinks we might expect more variability from station to station in this altitude regime. The high northern latitude stations have a range of increasing rates in the last decade (2008–2016) from EUR (0.08 ± 0.17%/yr) to NYA (0.30 ± 0.14%/yr). TAB has a recent rate of (1.55 ± 0.30%/yr) but is biased due to very high values in spring 2016 attributed to an anomalous local natural event. At and below the Arctic circle KIR clearly shows a minima in 2002 and an increase of (0.19 ± 0.08%/yr), the fore shortened series at STP shows a strong increase of (0.96 ± 0.14%/yr) and no trend at BRE (0.07 ± 0.07%/yr). Some northern mid-latitude stations show more to excessive variability for example, (PRS, TSK, and RKB) which may be due anthropogenic sources though notably quiescent in the northern mid-latitudes is BLD which would have less oceanic and possibly less anthropogenic influence. All northern mid-latitude stations show positive trends 2008–2016 of (0.11%–1.03%/yr) except BLD at (0.02 ± 0.10%/yr) and RKB due to a period of no data. In the subtropics PMB has a positive trend with (0.31 ± 0.13%/yr).

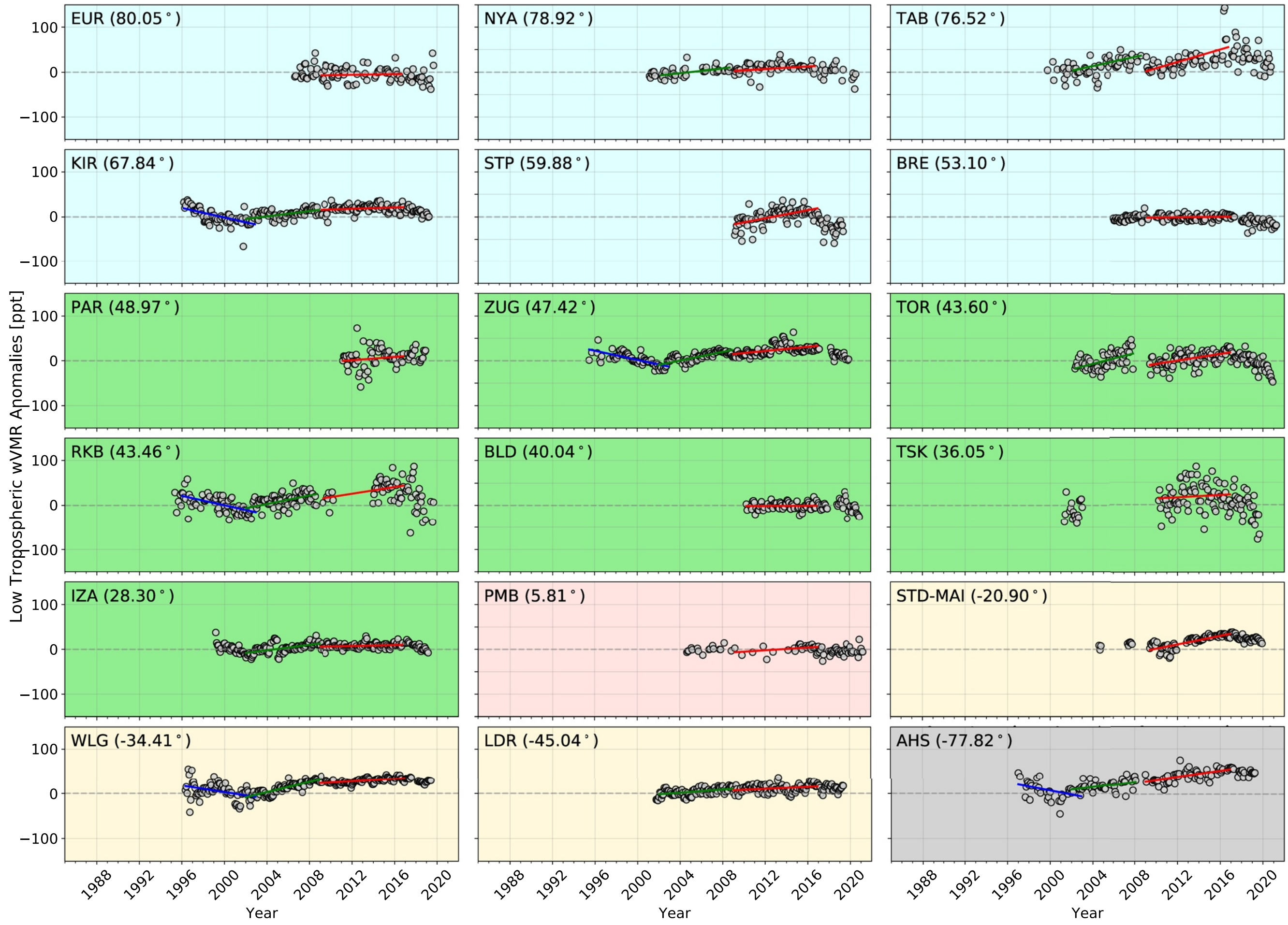

**Figure 8.** Time series of weighted OCS anomalies (wVMR) for the lower troposphere for all sites. Gray circles represent monthly mean anomaly. The blue line is the linear trend for period 1, green is for period 2, and red is for the most recent time period. See Equation 1 and text for definition of anomaly series.

The composite record from Saint Denis and Maïdo stations have a strong positive tropospheric trend of (1.01 ± 0.09%/yr) at higher southern latitudes. Anomalous inflections are clear in longer term records in the SH for example, LDR, WLG, and AHS as are trends, as seen in Kremser et al. (2015). These increase moving south at (0.19 ± 0.04%/yr), (0.24 ± 0.08%/yr), and (0.68 ± 0.12%/yr) at WLG, LDR, and AHS.

Figure 9 is similarly formatted as Figure 8 but for the FT (FT) monthly mean mixing ratios. The six high northern latitude station records all show a positive increase in the past decade. These range from (0.06 ± 0.05%/yr) at BRE to (0.87 ± 0.16%/yr) at TAB. Excluding TAB, the range is from 0.06 to (0.45 ± 0.12%/yr) at NYA. The high trend at TAB is primarily due to the high values seen in spring 2016. The longer term records in the Arctic have positive trends of (0.52 ± 0.06%/yr) at TAB (1999) and (0.38 ± 0.03%/yr) at KIR (1996). Of the northern mid-latitude stations PRS and BLD, their records show shallow non-significant trends while the others are all positive and range from (0.25 ± 0.04%/yr) at IZA to (0.76 ± 0.11%/yr) observed at TOR. Two long-term northern mid-latitude data records clearly show the minimum in 2002: ZUG (began 1995) and JFJ (began 1986). Prior to that, during the period 1996–2002, their trends were strongly negative at (−1.09 ± 0.12%/yr) and (−0.66 ± 0.04%/yr), respectively. The JFJ station has the longest data series, and although variability is larger in the earliest years, the downward, nearly linear trend clearly persisted since at least the inception of the record. The linear trend of the complete record for these two sites in the free troposphere are (0.34 ± 0.03%/yr) and (0.05 ± 0.02%/yr), respectively.

The subtropical stations have two at high altitude at ALZ and MLO. The ALZ time series begins in 2012 and has positive trend at (0.32 ± 0.13%/yr), while both PMB and MLO show stronger trends at (0.48 ± 0.14%/yr) and

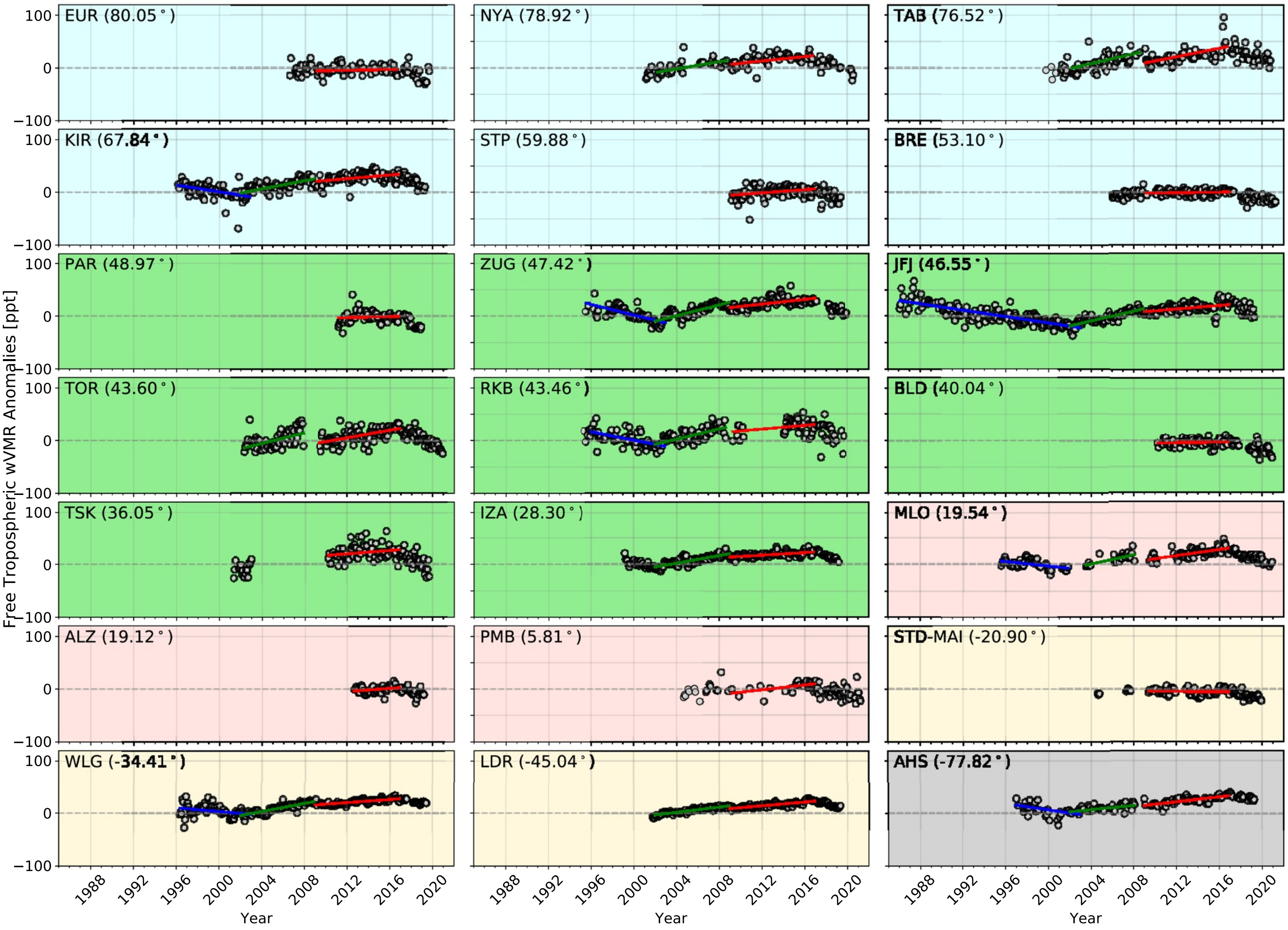

**Figure 9.** Time series of weighted OCS wVMR anomalies in the free troposphere for all sites. Annotated similarly as Figure 8.

(0.60 ± 0.08%/yr), respectively, although both, especially PMB, contain periods of sparse data in the observational record. The MLO station data series begins in 1995, the linear trend from that time is (0.31 ± 0.02%/yr). Of the four southern hemisphere stations STD-MAI shows a non-significant trend at (−0.02 ± 0.06%/yr), the others are positive in the past decade with (0.23 ± 0.02%/yr), (0.38 ± 0.03%/yr), and (0.45 ± 0.05%/yr) for WLG, LDR, and AHS, respectively. The two stations with the longest term records, at WLG (began 1996) and AHS (began 1997) have linear trends in the free troposphere of (0.28 ± 0.02%/yr) and (0.32 ± 0.02%/yr), respectively.

Although observations clearly show consistent trend fluctuations over the 36 yr (for JFJ and 26 yr for most other stations) FTIR record, globally, the FT OCS mixing ratio has increased between 0.05 (since 1986) or 0.28 (since mid-1990's) and 0.52%/yr. As noted above with regard to the total column time series, the very recent fall off since 2016–2017 is seen in several sites for example, ZUG, IZA, in the lower tropospheric time series. This is more clear and widespread in the FT data for example, TAB, KIR, JFJ, STD-MAI, LDR, and AHS.

Figure 10 is similarly formatted as Figure 8 but for the stratospheric (ST) monthly mean mixing ratios. For the three high arctic sites, two show positive trends for the past decade of (0.33 ± 0.27%/yr), (0.23 ± 0.24%/yr) for EUR, NYA but at TAB there is non-significant negative trend of (−0.28 ± 0.29%/yr). For the prior period 2002–2008 both NYA and TAB are strongly increasing by (1.13 ± 0.38%/yr) and (1.33 ± 0.58%/yr), respectively. The three next highest latitude sites show increases of (0.71 ± 0.30%/yr), (1.61 ± 0.30%/yr), and (0.81 ± 0.39%/yr) at KIR, STP, and BRE, respectively. Furthermore of the high northern mid-latitude sites that have longer term records TAB (1999) has a non-significant overall trend of (0.06 ± 0.12%/yr), and KIR (1996) at (0.26 ± 0.10%/yr). In the northern mid-latitudes, all eight stations show a positive increase in the 2008–2016 period ranging from (0.30 ± 0.23%/yr) at JFJ to (1.56 ± 0.52%/yr) at PRS, with PRS, BLD, and IZA all greater than

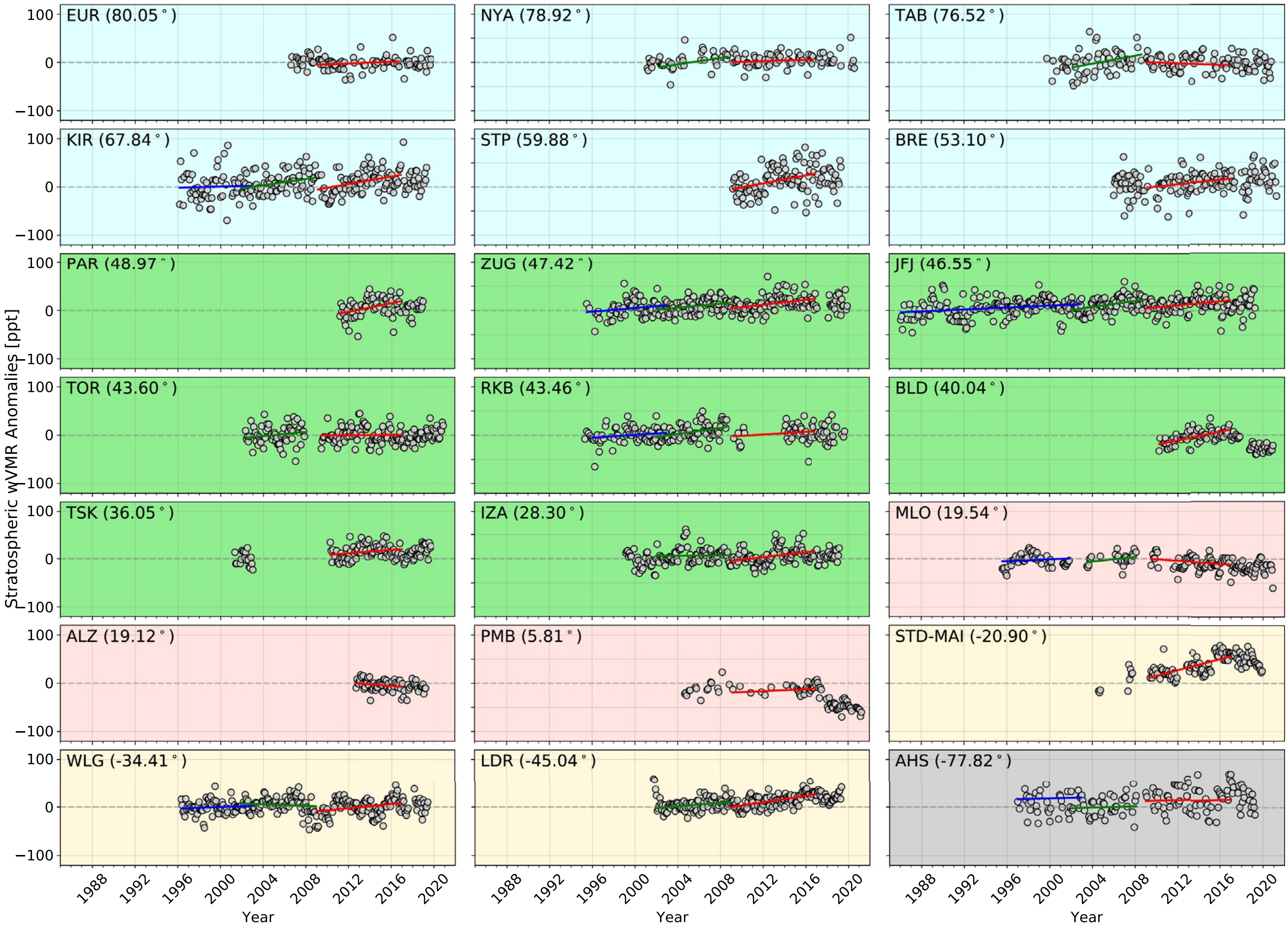

**Figure 10.** Time series of weighted OCS wVMR anomalies for the stratosphere component for all sites. Annotated similarly as Figure 8.

1%/yr. In the subtropics both MLO and ALZ show comparable negative rates of change at (−0.48 ± 0.20%/yr), (−0.54 ± 0.37%/yr), respectively, while the sparse PMB at 5.8°N shows an increase of (0.29 ± 0.16%/yr). Similarly all southern hemisphere stations show an increase of (1.93 ± 0.26%/yr), (1.01 ± 0.28%/yr), (1.12 ± 0.17%/yr), and (0.31 ± 0.58%/yr) at STD-MAI, WLG, LDR, and AHS, respectively.

The longest term linear trends of the stratosphere are slightly more varied. In central Europe the trend at JFJ since 1986 is (0.23 ± 0.04%/yr) while nearby at ZUG since 1995 it is higher at (0.35 ± 0.06%/yr). At high northern latitudes at KIR the positive trend is (0.26 ± 0.10%/yr) while higher at 70°N the trend at TAB is non-significant at (0.06 ± 0.12%/yr). In the subtropics, MLO shows a slight negative trend since 1995 at (−0.08 ± 0.04%/yr). In the southern hemisphere WLG has a non-significant trend of (0.04 ± 0.08%/yr) while at AHS at 79°S the trend since 1997 is (0.47 ± 0.15%/yr).

Generally the stratospheric mean monthly mixing ratios have more variability than the tropospheric values due in part to the increased uncertainty with this component of the retrieved profile. Nevertheless, of significance is the absence of the partial column fall off since ~2017 seen in both the lower and largely in the FT partial column time series at most sites. Given the tropospheric lifetime for OCS of ~2 to 3yr (Montzka et al., 2007), if the tropospheric trend continues it may be realized in the stratosphere in the near future.

### 3.2.1. Summary of Segmented Trends

A summary of the linear trends for the three atmospheric layers within three time periods since 1996 and for the several longest time series since inception is given in Figure 11. Figure 11a shows the trends for the longest term stations from their inception until 2016 for lower troposphere (red), free troposphere (blue), and stratosphere

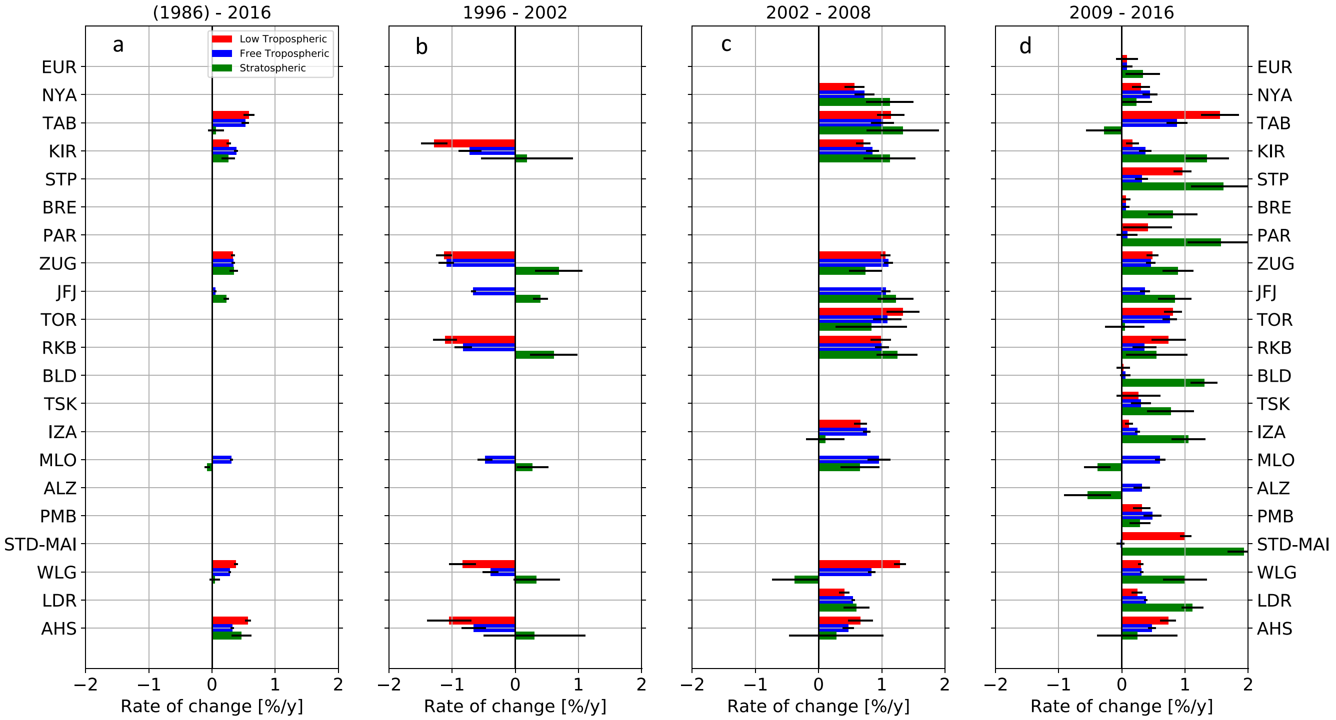

**Figure 11.** Trends by time period for all stations and for all three altitude ranges, listed by high to low latitude. Red represents the lower troposphere, blue the free troposphere, and green the stratosphere. The left panel (a) are trends for only those sites with data from 1996, then increasing time period left to right, (b) 1996–2002, (c) 2002–2008, and (d) 2009–2016 and so including more recently begun stations. Note, that the TAB dataset in the 1996–2016 panel begins in 1999, PRS dataset in panel 2009–2016 begins in 2011, and ALZ dataset in panel 2009–2016 begins in 2012.

(green). Figure 11b are the linear trends until 2002 for stations that begin at latest in 1996 (1999 TAB). Figure 11c similar as Figure 11b until 2008 for stations starting at latest in 2002 and Figure 11d are the latest trends from 2008 to 2016. Figure 11a shows the seven longest running time series trends which range from non-significant up to (0.58 ± 0.09%/yr) at TAB. From Figure 11b: of the 8 yr leading to 2002 all tropospheric trends are strongly decreasing from (−0.39 ± 0.13%/yr) at WLG in the free troposphere to (−1.29 ± 0.20%/yr) KIR in the lower troposphere. During this time all stations have positive stratospheric trends, although they are non-significant in the southern hemisphere and KIR at 67°N. Figure 11c shows a general reversal in tropospheric trends with continued positive stratospheric trends in the northern latitudes but variable in the south. Tends in Figure 11c are mostly positive and strong on the stratosphere except in the subtropics where they are negative.

### 3.3. FT Trends and Proxy Regression

The basis for the segmented linear regions are the consistent inflection points for the longest term data series illustrated in Figure 7 and seen more clearly in the FT anomaly data series in Figure 9. To attempt to define drivers of this multi-year variability, a two-part regression approach is applied to the FT anomaly time series isolating proxies by zonal bands given in Table 3. The first step uses a Stepwise Multiple Regression (SMR; Appenzeller et al., 2000; Bahramvash Shams et al., 2019; Brunner et al., 2006; Kivi et al., 2007; Vigouroux et al., 2015) where the contribution of proxies are investigated for each site to determine a dominant set for the stations to be used in the second regression run for all sites in that zone (Bahramvash Shams et al., 2019; Wohltmann et al., 2007). This method avoids spurious correlation of proxies and OCS (Wohltmann et al., 2007). Forward selection criteria are the highest explained variance ($R^2$) and $p$-value lower than 0.05 of the SMR (Section 7.4.2 of Wilks, 2011). The iteration converges when no variable can increase the $R^2$ by more than 1%.

Proxies are chosen from available monthly indexes and global satellite datasets to attempt to capture characteristics defining atmospheric OCS including its long lifetime, the complex sources and sinks. Taking advantage of the SMR's ability to exclude less relevant proxies we chose a range of available biological and geophysical proxies that are listed in Table 7. These include large scale dynamical processes: quasi-biennial oscillation (QBO), Arctic

**Table 7**
*Proxy, Description, and Source for Proxy Data for FT SMR-COC Regression Analysis*

| ID | Name | Description | Source |
|---|---|---|---|
| QBO | Quasi-biennial oscillation | Based on equatorial stratosphere winds at 30 and 10 hPa | http://www.geo.fuberlin.de/en/met/ag/strat/produkte/qbo/index.html |
| AO | Arctic oscillation | Monthly values from NCEP | http://www.cpc.ncep.noaa.gov/products/precip/CWlink/daily_ao_index/ao.shtml |
| ENSO | El Niño/Southern Oscillation index | Multivariate El Niño/Southern Oscillation index (MEI) | http://www.esrl.noaa.gov/psd/enso/mei/ |
| NDVI | Normalized Difference Vegetation Index | MODIS/Terra Vegetation Indices, Monthly L3 Global 0.05° (MOD13C2) Version 6. | https://lpdaac.usgs.gov/products/mod13c2v006/ |
| CHLOR | Chlorophyll index | Monthly values from MODIS/Aqua at 4 km resolution | https://oceancolor.gsfc.nasa.gov/ |
| SST | Sea Surface Temperature | Monthly values from MODIS/Aqua using the 1 and 12 μm bands at 4 km | https://oceancolor.gsfc.nasa.gov/ |
| SIC | Sea ice Concentration | National Climatic Data Center Monthly mean analyses | https://rda.ucar.edu/datasets/ds277.0/index.html#!description |

oscillation (AO), and the El Nino/Southern oscillation (ENSO), proxies related to terrestrial and ocean fluxes Whelan et al. (2018), Normalized Difference Vegetation Index (NDVI; Kettle et al., 2002) and Chlorophyll index (CHLOR), sea surface temperatures (SST; Lennartz et al., 2017) sea ice concentration (SIC; Becagli et al., 2016).

To conserve the local variability of SST, 11 SST regional averages are estimated for use in the SMR. Zonally averaged NDVI and CHLOR use latitude ranges as in Figure 3. Multivariate ENSO Index (MEI), time lag of 0–4 months are used (Bahramvash Shams et al., 2019; Randel et al., 2009; Vigouroux et al., 2015). However, the selection process will remove all but at most one. The resulting correlation coefficients among variables are <40% except for regional MEI with tropical SST (20°S–20°N) and where only SST is used in the final model. This regression is applied to a subset of data and proxies that overlap in the time period 2004–2017 and due to the short MAI time series, it is excluded. Selected mutual proxies are similar for LT and FT so the final regression is given for the FT anomalies. SST is a mutually selected proxy in all regions. NDVI is found to be dominant in the sub-tropics and all northern zonal bins, MEI in the north mid-latitude (20°–50°N) only and sea ice extent in the Arctic (50°–90°N) only.

Due to long lifetime of OCS, we expect a high degree of autoregressive structure in OCS time series. The Cochrane-Orcutt correction (COC) is applied in the final model (Cochrane & Orcutt, 1949). The results of the final regression are shown in Figure 12. They emphasize the accumulation of OCS seen in the improvement of $R^2$ with application of the COC. Using COC the selected variables are able to explain the fluctuations of the anomalies FT OCS time series by $R^2$ more than 78% in 16 of 21 stations as shown in the upper left of each station panel in Figure 12.

Excluding the COC, the geophysical and biogenic proxies can at most cumulatively account for 32% of variability but much lower at most stations. A recently revised anthropogenic emissions inventory is shown in Figure 2 of Zumkehr et al. (2018) but is currently only available for 1980–2012 on an annual basis and was not included in the SMR above due to the mismatch in data overlap and granularity. Using stations with at least 12 yr of overlap, a single annual regression with no auto-correlation correction was performed. The results are shown in Figure 13. ZUG with $R^2 = 66\%$, TAB at 56%, and WLG at 46% with the lowest correlation coefficients here, are all higher than all other proxies combined in the monthly SMR analysis. All other correlations have $R^2 > 70\%$ with LDR at 77%. The Zumkehr et al. (2018) record ends in 2012, though the observational records here show a clear continued increase to ~2016 to 2017 followed by a period of rapid decline to 2020. Given the correlations to biogenic, oceanic, and anthropogenic proxies above, there is a high degree of confidence the FT OCS concentrations are most strongly influenced by anthropogenic sources since at least the mid-1980's. Details of the components of the anthropogenic emissions inventory are given in Zumkehr et al. (2018). Given these strong correlations and the decreases in OCS since ~2017, we may expect that this decrease too, is due to a slowdown in anthropogenic emissions.

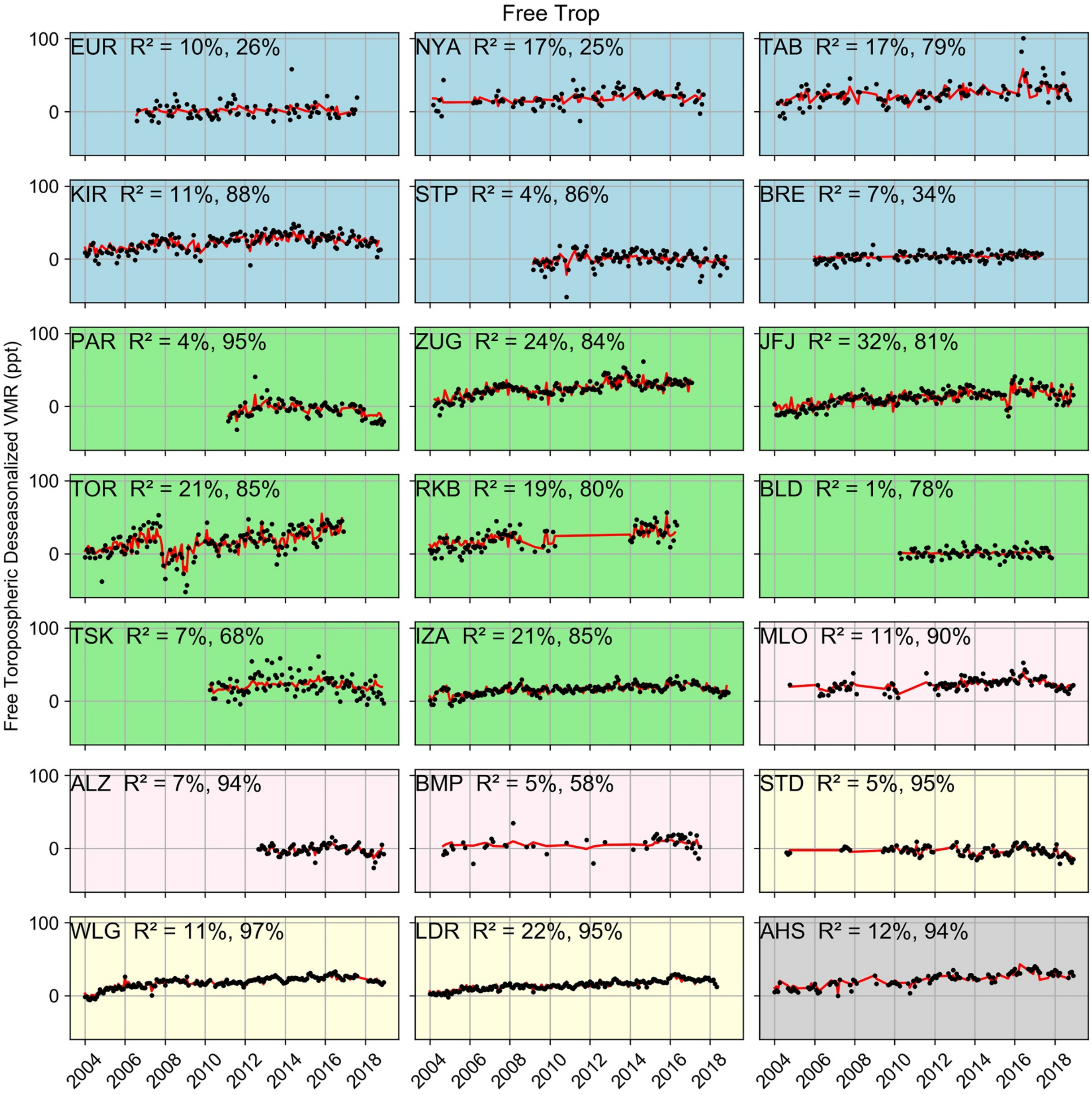

**Figure 12.** Final fit of dominant meridional and zonal proxies to free tropospheric anomalies using the Cochrane-Orcutt auto-regression analysis. $R^2$ with and without auto-regression are shown in upper left of the plot for each station.

### 3.4. Stratospheric Trends Using a Dynamical Proxy Regression

OCS flux to the stratosphere is an important contributor to the stratospheric aerosol layer (Kremser et al., 2016) and the long term trend of stratospheric OCS concentration can affect the maintenance of the aerosol layer over time. Stratospheric $N_2O$ has been shown to be effective as a proxy to attempt to account for stratospheric dynamical effects that would effect all long lived trace species and so diminish the variations in the trend of a stratospheric species (Rinsland et al., 2008; Stolarski et al., 2018; Toon et al., 2018). $N_2O$ is a standard retrieval species within the NDACC IRWG and available at the NDACC Data Handling Facility (DHF) for all stations (Zhou et al., 2019). $N_2O$ time series are retrieved in a standardized manner using the same forward model and on the same retrieval grid as the OCS (see www.acom.ucar.edu/irwg/links) across the network to form a globally harmonized data product. For this work the retrieved $N_2O$ profiles were processed identically as the OCS to produce a co-located monthly mean stratospheric $N_2O$ wVMR time series. The stratospheric $N_2O$ time series given

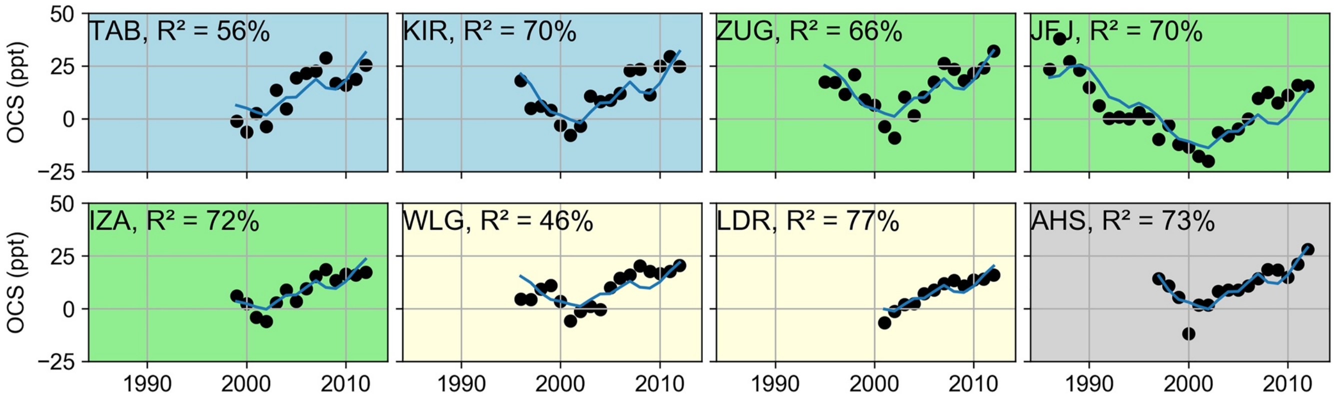

**Figure 13.** Fit to the annual anthropogenic emissions inventory from Zumkehr et al. (2018) to the annual average of the FT time series at stations with the longest running data records. The emissions inventory is interpolated to the station location. ZUG with $R^2 = 66\%$, TAB at 56%, and WLG at 46% at the lowest values are all higher than all other proxies combined. All other correlations have $R^2 > 70\%$.

by $P_{N_2O}$ in Equation 3 is used as a regression proxy for the longest term stations. Since $N_2O$ has been increasing at ~0.25%/yr (Stolarski et al., 2018), $P_{N_2O}$ is decreased at this rate rendering $a_1$ the linear trend of OCS after fitting.

$$\begin{aligned} f_{N_2O}(x) &= a_0 + a_1 x + b_0 P_{N_2O}(x) \\ x &= t - t_0 \end{aligned} \tag{3}$$

To allow a direct global comparison from the stations with the longest data records still representing a wide range of latitudes, the trends given here use the same time series duration of 2001–2016 for all stations. The results of this process on the regression and trends are shown in Figure 14. Generally the process improves the $R$-values compared in Figure 14a, for all stations except for MLO and LDR. Figure 14b shows only slight changes in residuals that are all improved except for LDR. Figure 14c compares the trends with the straight long-term linear regression where most trends increase though within uncertainties, which includes MLO that becomes less negative. WLG becomes much more negative and LDR slightly more though both still within uncertainties.

Based on these long-term regressions northern mid-latitude to Arctic stratospheric trends are increasing from (0.12 ± 0.09%/yr), (0.32 ± 0.12%/yr), (0.25 ± 0.07%/yr), (0.28 ± 0.09%/yr), (0.28 ± 0.11%/yr) at TAB, KIR, ZUG, JFJ, and IZA, respectively. At 19.5°N and −34.4°S the stratospheric trends are negative at (−0.10 ± 0.07%/yr)

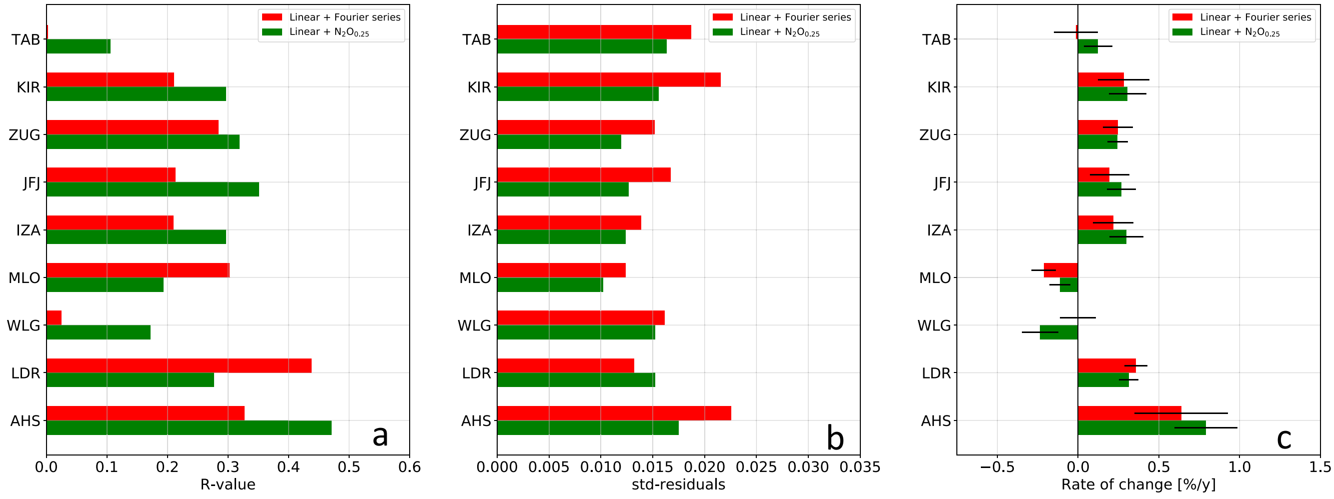

**Figure 14.** Results of the $N_2O$ proxy analysis on the longest stratospheric data records from 2001 to 2016. (a) $R$-values of the regression and show generally higher correlations except for MLO and LDR. (b) The comparison of fit residuals showing slightly improved regressions using the $N_2O$ proxy. (c) Compares the linear trends. Using the $N_2O$ proxy most trends are slightly increased except WLG and LDR but all within uncertainties.

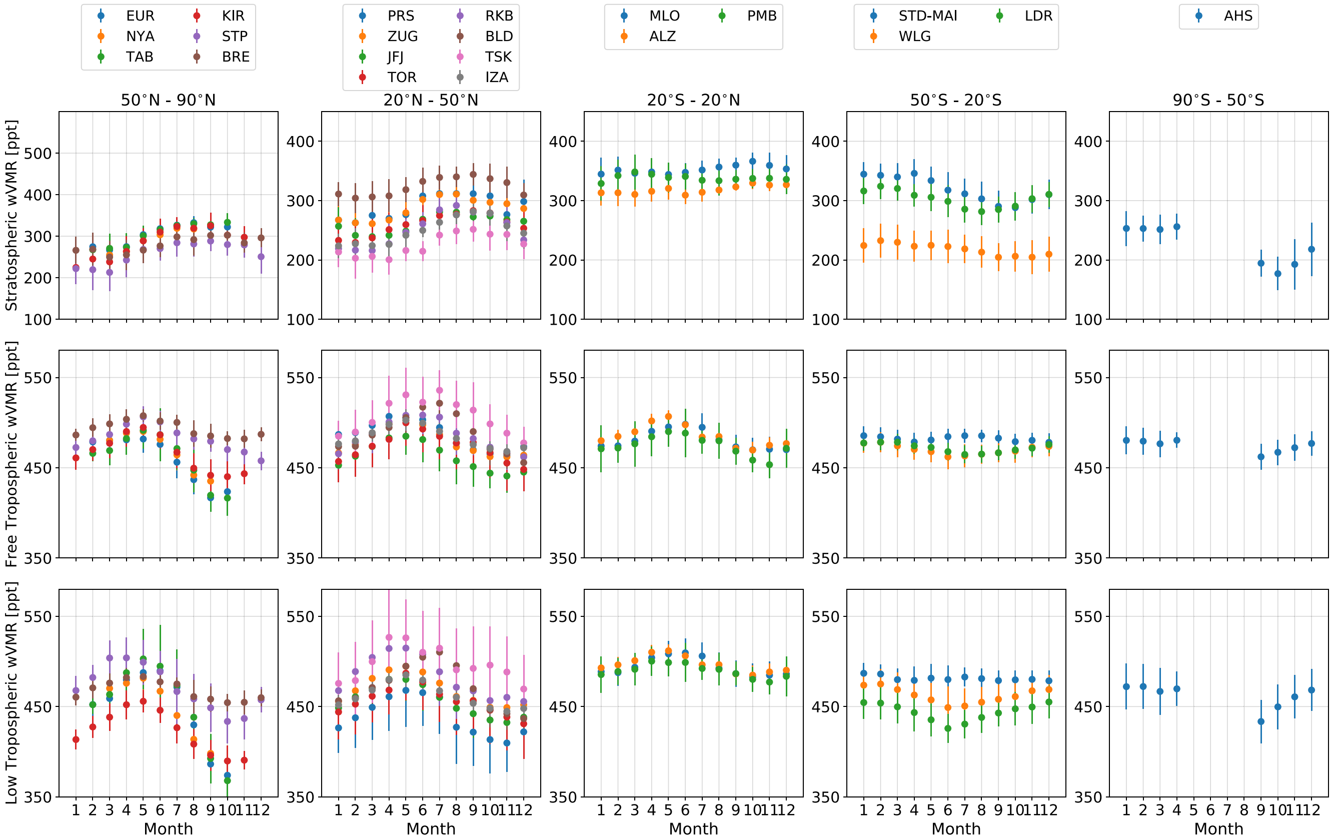

**Figure 15.** Annual cycle using monthly mean wVMR for all stations. Panels left to right are decreasing latitude bins (see Table 3) and increasing altitude bins bottom to top. All data are used irrespective of station time series duration.

and (−0.24 ± 0.12%/yr) at MLO and WLG, respectively. LDR has similar positive rate to northern mid-latitudes at (0.27 ± 0.06%/yr) and the largest increase is seen at AHS of (0.79 ± 0.19%/yr). This represents a strong accumulation of stratospheric OCS in the Antarctic in recent years that appears to not be represented in the analysis of Kremser et al. (2016) in which trends ended in 2016.

### 3.5. Annual Cycles

Monthly seasonal variations of wVMR with $\pm 1\sigma$ of the average are presented in Figure 15. These represent a global view of the seasonality of atmospheric OCS. The FTIR monthly means are color coded by site (see legends) and presented for the three layers and latitude bins. Tropospheric cycles at Arctic stations show a large annual change from highs near 500 pptv in late spring at EUR, NYA, and TAB to lows below 370 pptv in late summer. Recently de-iced oceanic sources may account for excess spring amounts (Becagli et al., 2016). If high Arctic tropospheric concentrations are driven by oceanic sources lower fall emission may account for the minima in October. This is different from the more sustained high concentrations on the European continent at BRE and STP. Of note is the larger year to year range seen at STP as opposed to BRE pointing to more varied local sources or sinks. In the stratosphere all high latitude sites peak in September or October with maxima between 280 and 340 pptv increasing poleward.

At northern mid-latitudes in the LT the peak in the cycle for TSK, RKB is in April, for PRS it is May–June, for BLD it is June–July, and for the other sites it is May. TSK, while it exhibits the largest variability also has a secondary peak in October. While PRS has a large drop from 460 pptv in July to 425 in August. Minimum values are in late fall after a steady decline through the summer commensurate with an expected drawdown due to plants without other significant sources. In the FT aside from TSK which maintains high values from April to September and BLD which peaks in July, all other sites peak in June. Northern mid-latitude stratospheric values show the largest range in OCS mixing ratios in longitude with BLD maintaining the highest values of up to 340 pptv in

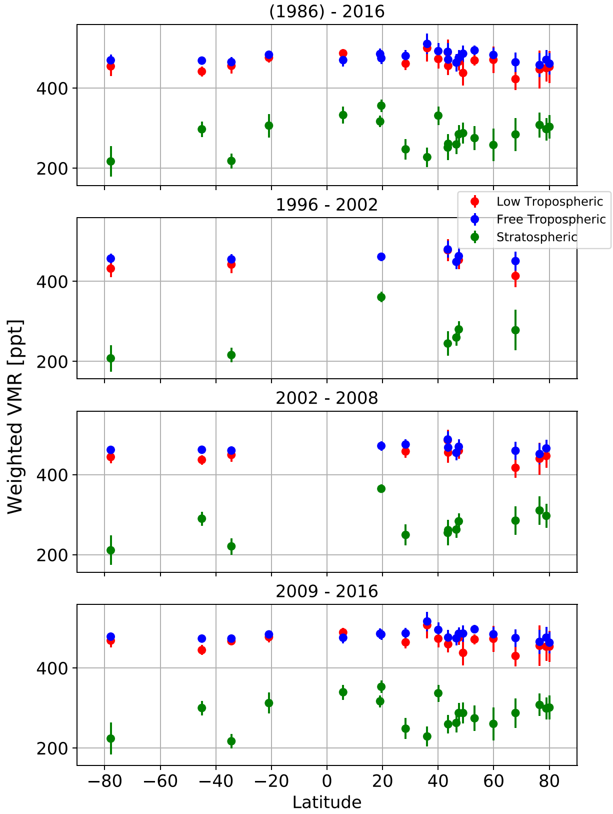

**Figure 16.** All wVMR data vs. latitude and panels represent estimated monotonic trend periods. Color codes are green: stratosphere, blue, free troposphere, and red is the lower troposphere.

summer and fall months and TSK peaking at 240 ppt. The BLD time series is short, recently starting in 2010 which may tend to bias towards higher averaged wVMR's. Annual variations are on the order of 50 pptv.

The three tropical sites do not well characterize the longitudinal space (see Table 1). Both the LT and FT have a maximum in May. PMB has a minimum in November while ALZ and MLO have minima in October. MLO tends to maintain low values through to February while ALZ rebounds and PMB appears to in December but has limited observations due to seasonal cloud cover. Shallow seasonal cycles seen in subtropical stations in the troposphere are likely due to minimal seasonal changes in oceanic sources. LS values above 300 pptv are maintained throughout the year as there is a small seasonal cycle amplitude of 20 pptv. ALZ and MLO tend to see highest values in September while PMB has highest monthly means in February.

Similarly the three lower mid-latitude sites do not well characterize the longitudinal space and as in the tropical zone reflect a limitation of the network. In the LT STD-MAI in the Indian Ocean sees little seasonal variation but fairly high sustained values year round between 460 and 480 pptv. Both LDR and WLG further East and South and on much larger land masses show clear similar cycles with peaks in January–February and minimums in early winter in June. LDR shows a concentration of about 30 pptv lower for all months and reveals a distinct latitudinal gradient South from the tropical sites. In the FT there is very shallow cycle that is similar for WLG and LDR, but at STD-MAI peaks in January and July–August are observed. In the LS the lower latitude site at STD-MAI has the highest values from January to April then decreasing by as much as 70 pptv in September. LDR is similar but with a shallower amplitude. WLG sees a much lower mean value between 200 and 250 pptv. In the Antarctic, AHS sees considerable variability year over year in the LT and low values above 400 pptv that never are as low as in the Arctic for example, EUR and TAB at 360 and 370 pptv in the autumn. Rather AHS sees it highest FT values just before winter. FT values are very similar to southern mid-latitude values. Spring values are the lowest LS values seen at 160 pptv in September likely when subsidence still effects the LS. Summer and autumn values are consistent at about 240 pptv.

This global dataset shows some remarkable seasonality such as the low values in LT at the highest northern latitude stations even contrasted with stations between 50° and 60°N, the large range in seasonal and year to year variability in northern mid-latitudes LT and TSK, though with high variability, shows a second peak in the fall that is not seen at other stations. Finally the contrast between the northern and southern hemisphere seasonal amplitude points to systemic differences in sources Notholt et al. (2006), Montzka et al. (2007), and Berry et al. (2013).

### 3.6. Latitudinal Variation

The latitudinal distribution of all mean OCS wVMR data are plotted in Figure 16. The upper panel are all data for each station and the lower panels are for each estimated monotonic trend period. Vertical bars represent $\pm 1\sigma$ and largely reflect the seasonal cycles shown in Figure 15. Owing to the tropospheric lifetime all FT mean values range higher than the lower tropospheric values, except between 0° and 20°N where they are slightly reversed. This may point to a relatively larger net source in the Northern tropics as proposed, for example, Berry et al. (2013) and Launois et al. (2015), though this is not seen further from the equator at IZA at 28°N. There are several stations between 30° and 60°N that range from Japan, North America (NA), and Europe, where there is small decrease in OCS in the free troposphere and more so in lower troposphere. This persistent feature generally reproduces the in situ measurements given in Montzka et al. (2007) for NA, show that this effect is more global and may reflect a net continental sink.

**Table 8**
*Calculations of the Stratospheric Lifetimes of OCS Using Equation 4 and Measured FT OCS and $N_2O$ Concentrations Across the Five Latitude Bands*

| Latitude band [°N] | *A* [ppb/ppb] | Mean FT OCS [ppb] | Mean FT $N_2O$ [ppb] | $R^2$ | Average lifetime [yr] |
|---|---|---|---|---|---|
| 90 to 50 | 482.9 ± 6.8 | 0.472 ± 0.028 | 315.8 ± 10.8 | 0.79 | 84.5 ± 15.6 |
| 50 to 20 | 327.3 ± 4.6 | 0.483 ± 0.020 | 318.4 ± 5.3 | 0.86 | 58.0 ± 10.3 |
| 20 to −20 | 309.3 ± 13.4 | 0.477 ± 0.016 | 319.4 ± 4.5 | 0.83 | 54.1 ± 9.7 |
| −20 to −50 | 448.1 ± 10.2 | 0.468 ± 0.012 | 314.3 ± 6.7 | 0.90 | 78.1 ± 13.7 |
| −50:−90 | 577.6 ± 20.9 | 0.475 ± 0.008 | 310.2 ± 6.2 | 0.89 | 103.4 ± 18.3 |

Tropical sites show the highest stratospheric wVMR values between 300 and 360 pptv. These tend to fall in lower mid-latitudes than increase poleward in the NH where the Arctic sites maintain values of 300–310 pptv. There are fewer stations in the SH but the long-term site an AHS has a suppressed value of 220 pptv in the stratosphere.

### 3.7. Atmospheric Lifetime of OCS

Each site measures vertical profiles of $N_2O$ as a standard data product as discussed with regards to dynamical proxies. Using tracer-tracer correlations for tropospheric source species that are in FT steady state with sinks only in the stratosphere as defined in Plumb and Ko (1992) and employed by Krysztofiak et al. (2015) the lifetime for LS OCS can be calculated with Equation 4.

$$\frac{\tau_{OCS}}{\tau_{N_2O}} = A \cdot \frac{wVMR_{OCS}}{wVMR_{N_2O}} \tag{4}$$

where $\tau$ is the respective species lifetime in years. Using monthly means, $A$ is the linear correlation of the measured FT concentrations of $N_2O$ and OCS using an orthogonal regression and propagating the uncertainties from the standard deviations of the monthly averages for both species. The wVMR are the respective measured LS monthly mixing ratios. The FT lifetime of $N_2O$ used is (117 ± 20)yr from Montzka and Fraser (2003). This was performed for all sites and binned by latitude as defined in Table 3. Calculations and results for the global estimate of LS OCS lifetime using all data are summarized in Table 8.

The latitudinal lifetime distribution show a clear increase poleward. At high latitudes the (84.5 ± 15.6)yr calculated here is longer then the mean from several measurement sets of (71 ± 10)yr found in Krysztofiak et al. (2015) although within error bars. The data here include three datasets at 76°N and higher latitudes which extend northward the reach from the previous balloon-borne datasets. The longest lifetime is recorded in the (−50° to −90°) zonal bin but composed of the single site at AHS.

## 4. Conclusions

This discussion seeks to show the long-term trends in OCS the largest reservoir of tropospheric sulfur and sulfur source to the stratosphere where it plays an important role in maintaining the stratospheric sulfate aerosol layer. We presented atmospheric OCS time series data from 1986 (earliest) to 2020 from 22 globally distributed, from 80°N to 79°S, ground-based remote-sensing high-resolution NDACC FTIR stations. We developed a globally consistent retrieval analysis including measurement based a priori data to produce homogenous retrievals that were performed by each station managing group. These OCS vertical mixing ratio profiles were cast into partial columns and reduced to mean weighted mixing ratios then time averaged to represent mean monthly mixing ratios in the lower and free troposphere and lower stratosphere for globally consistent analysis.

This analysis showed that changes in trends on multi-year to decadal scales described in earlier reports are global features seen at other latitudes at stations with records of sufficient duration due to the long OCS lifetime. In particular the longest records at KIR, ZUG, JFJ, MLO, WLG, and AHS show linear decreases from inception to the early 2000's revealed in the low and FT anomaly time series. Further, changes in trend are seen ~2008 and then in the 2016–2019 period. To elucidate these changes we present linear trends during these periods in each altitude layer. We have obtained data for most stations up through 2019 or 2020. At about the 2016–2017 time period and later all stations show a down turn in trend in the free troposphere. This most recent linear time regime is short and limited conclusions should be drawn. But given the tropospheric lifetime of OCS of ~2 to 3 yr, if the tropospheric trend continues it may be realized in the stratosphere in the near future.

Two regressions were used to investigate the drivers of FT OCS concentration due to the time overlap and granularity of data and proxies. A two-step SMR approach defined important proxies and the COC correction accounted for the accumulation of OCS. Results show the relative the importance of SST at all zones, NDVI at northern hemisphere and tropical regions, MEI at northern high latitudes, and sea ice extent at northern high latitudes. Using SMR-COC approach, FT fluctuations of OCS are reproduced with an $R^2$ higher than 78% in most of the study sites though without COC $R^2$ ranged from 4% to 32%. Separately due to proxy and observational data overlap and granularity the, FT time series at eight of the longest time series over a wide range of latitudes show high correlations with an $R^2 =$ ranging from 46% to 77% with the revised anthropogenic emissions budget of Zumkehr et al. (2018) between 1986 and 2012. We conclude this has had the largest effect on the LT and FT trends variability since 1986 and that a slowing of anthropogenic emissions is likely the cause of the recent negative trends in FT OCS.

Stratospheric anomalies do not show the recent change since ~2017 to 2019. In the north and south mid-latitudes since 2008 increases are seen. At high northern latitudes there are small non-significant trends. AHS shows a positive change but with large uncertainty. This is in contrast to the negative trends at MLO and ALZ. Linear trends were calculated for the stratosphere with the anomaly data and by using retrieved $N_2O$ stratospheric partial column data as a dynamical proxy. The comparison in trends for stations with records from 2001 to 2016 show a general improvement using the regression and slightly increased the trends with some exceptions. The trend at both WLG and LDR decreased. Nevertheless, globally northward of MLO and southward of WLG stratospheric trends have been increasing since 2001, 0.12%–0.32%/yr and 0.27%–0.79%/yr, respectively. This infers an excess of stratospheric sulfur over time and that the limiting factor to conversion to sulfate aerosol may not be sulfur derived from OCS. For the conditions of a steady state aerosol loading, the case may be more clear but given the uncertainty in total loading and its variability (Kremser et al., 2016) a stronger conclusion cannot be made from these observations.

Although this dataset is limited to 22 globally disperse locations, aside from the density of stations in continental Europe, the duration of the time series records and continuity of observations characterizes this as the most thorough global dataset of atmospheric carbonyl sulfide available. The dataset clearly show that the trend in OCS varies especially in the troposphere. That there is overall a small but increasing trend in the stratosphere seen in the longest time series except MLO 19.5°N and WLG at −34.4°S. Also that the trends in most of the atmosphere was increasing in the period 2008–2016 but that this trend seen in the tropospheric data to 2020 is now decreasing at all stations.

## Data Availability Statement

The OCS and $N_2O$ time series data are currently an NDACC IRWG standard data product, they are archived at the NDACC DHF at www.ndacc.org and are available to the public. SMR proxy data are available at addresses given in Table 7 and the anthropogenic proxy data are previously published (Zumkehr et al., 2018).

**Acknowledgments**
The authors wish to thank S. Kremser (Bodeker Scientific Inc.) for many useful conversations concerning OCS and stratospheric aerosols. The National Center for Atmospheric Research is sponsored by the National Science Foundation. The NCAR FTS observation programs at Thule, Greenland, Boulder, CO, USA and Mauna Loa, HI, USA are supported under contract by the National Aeronautics and Space Administration (NASA). The Thule work is also supported by the NSF Office of Polar Programs (OPP). We

## References

Appenzeller, C., Weiss, A. K., & Staehelin, J. (2000). North Atlantic oscillation modulates total ozone winter trends. *Geophysical Research Letters*, *27*(8), 1131–1134. https://doi.org/10.1029/1999GL010854

Bahramvash Shams, S., Walden, V. P., Petropavlovskikh, I., Tarasick, D., Kivi, R., Oltmans, S., et al. (2019). Variations in the vertical profile of ozone at four high-latitude arctic sites from 2005 to 2017. *Atmospheric Chemistry and Physics*, *19*(15), 9733–9751. https://doi.org/10.5194/acp-19-9733-2019

Barkley, M. P., Palmer, P. I., Boone, C. D., Bernath, P. F., & Suntharalingam, P. (2008). Global distributions of carbonyl sulfide in the upper troposphere and stratosphere. *Geophysical Research Letters*, *35*(14), L14810. https://doi.org/10.1029/2008GL034270

Becagli, S., Lazzara, L., Marchese, C., Dayan, U., Ascanius, S., Cacciani, M., et al. (2016). Relationships linking primary production, sea ice melting, and biogenic aerosol in the Arctic. *Atmospheric Environment*, *136*, 1–15. https://doi.org/10.1016/j.atmosenv.2016.04.002

Berry, J., Wolf, A., Campbell, J. E., Baker, I., Blake, N., Blake, D., & Zhu, Z. (2013). A coupled model of the global cycles of carbonyl sulfide and co2: A possible new window on the carbon cycle. *Journal of Geophysical Research: Biogeosciences*, *118*(2), 842–852. https://doi.org/10.1002/jgrg.20068

wish to thank the Danish Meteorological Institute for support at the Thule site and NOAA for support at the MLO site. The Eureka measurements were made at the Polar Environment Atmospheric Research Laboratory (PEARL) by the Canadian Network for the Detection of Atmospheric Change (CANDAC), and the Toronto measurements were made at the University of Toronto Atmospheric Observatory (TAO); both are primarily supported by the Natural Sciences and Engineering Research Council of Canada (NSERC), the Canadian Space Agency (CSA) and Environment and Climate Change Canada (ECCC). The Paris station has received funding from, Sorbonne Université; the French Research Center CNRS, the French Space Agency CNES, and Région Île-de-France. The Jungfraujoch FTIR monitoring program has received funding from the F.R.S.-FNRS (under grants J.0147.18 and J.0126.21), the Fédération Wallonie-Bruxelles, both in Brussels, Belgium, and from the GAW-CH program of MeteoSwiss. EM is a senior research associate with F.R.S.-FNRS. Alejandro Bezanilla is acknowledged for measurements and data managements of the Altzomoni Site and Alfredo Rodriguez, Delibes Flores, Omar Lopez, and Eugenia Gonzalez de Castillo are acknowledged for technical support. The Observations in Mexico are founded by the grants CONACYT-290589 and PAPIIT-IN111521. RUOA-Network https://www.ruoa.unam.mx/ is acknowledged by supporting the infrastructure of the Altzomoni Observatory and the administration of the National Park Izta-Popo Zoquiapan are acknowledged for hosting and supporting this site. KIT, IMK-ASF would like to thank Uwe Raffalski and Peter Voelger from the Swedish Institute of Space Physics (IRF) for their continuing support of the NDACC FTIR site Kiruna. FTIR measurements at Lauder and Arrival Heights are core-funded by NIWA (programme CAAC_2201) through New Zealand's Ministry of Business, Innovation and Employment Strategic Science Investment Fund. We also thank Antarctica New Zealand for providing logistical support for the FTIR measurements at Arrival Heights. The University of Bremen team acknowledge the AWI Bremerhaven, Germany, and the personnel at the AWIPEV research base in Ny Ålesund, Svalbard, for logistical and on-site support. This publication has been supported by the senate of Bremen, the BMBF (Federal Ministry of Education and Research, Germany) in the ROMIC-II subproject TroStra (FKZ: 01LG1904A) and the DFG (German research foundation in the Transregio 172, Arctic Amplification, project number 268020496, subproject E02). The Izaña FTIR station has been supported by the German Bundesministerium für Wirtschaft und Energie (BMWi) via DLR under grants 50EE1711A and

Boone, C. D., Walker, K. A., & Bernath, P. F. (2013). Version 3 retrievals for the atmospheric chemistry experiment Fourier transform spectrometer (ACE-FTS). In P. F. Bernath (Ed.), *The atmospheric chemistry experiment ace at 10: A solar occultation anthology* (pp. 103–127). A. Deepak Publishing.

Brühl, C., Lelieveld, J., Crutzen, P. J., & Tost, H. (2012). The role of carbonyl sulphide as a source of stratospheric sulphate aerosol and its impact on climate. *Atmospheric Chemistry and Physics*, *12*(3), 1239–1253. https://doi.org/10.5194/acp-12-1239-2012

Brunner, D., Staehelin, J., Maeder, J. A., Wohltmann, I., & Bodeker, G. E. (2006). Variability and trends in total and vertically resolved stratospheric ozone based on the CATO ozone data set. *Atmospheric Chemistry and Physics*, *6*(12), 4985–5008. https://doi.org/10.5194/acp-6-4985-2006

Buchholz, R. R., Deeter, M. N., Worden, H. M., Gille, J., Edwards, D. P., Hannigan, J. W., et al. (2017). Validation of MOPITT carbon monoxide using ground-based Fourier transform infrared spectrometer data from NDACC. *Atmospheric Measurement Techniques*, *10*(5), 1927–1956. https://doi.org/10.5194/amt-10-1927-2017

Campbell, J. E., Berry, J. A., Seibt, U., Smith, S. J., Montzka, S. A., Launois, T., et al.(2017). Large historical growth in global terrestrial gross primary production. *Nature*, *544*, 84–87. https://doi.org/10.1038/nature22030

Campbell, J. E., Whelan, M. E., Seibt, U., Smith, S. J., Berry, J. A., & Hilton, T. W. (2015). Atmospheric carbonyl sulfide sources from anthropogenic activity: Implications for carbon cycle constraints. *Geophysical Research Letters*, *42*(8), 3004–3010. https://doi.org/10.1002/2015GL063445

Cochrane, D., & Orcutt, G. H. (1949). Application of least squares regression to relationships containing auto-correlated error terms. *Journal of the American Statistical Association*, *44*(245), 32–61.

Coffey, M. T., & Hannigan, J. W. (2010). The temporal trend of stratospheric carbonyl sulfide. *Journal of Atmospheric Chemistry*, *67*, 61–70. https://doi.org/10.1007/s10874-011-9203-4

Crutzen, P. J. (1976). The possible importance of CSO for the sulfate layer of the stratosphere. *Geophysical Research Letters*, *3*, 73–76. https://doi.org/10.1029/GL003i002p00073

Dammers, E., Shephard, M. W., Palm, M., Cady-Pereira, K., Capps, S., Lutsch, E., et al. (2017). Validation of the CrIS fast physical $NH_3$ retrieval with ground-based FTIR. *Atmospheric Measurement Techniques*, *10*(7), 2645–2667. https://doi.org/10.5194/amt-10-2645-2017

De Mazière, M., Thompson, A. M., Kurylo, M. J., Wild, J. D., Bernhard, G., Blumenstock, T., et al. (2018). The network for the detection of atmospheric composition change (NDACC): History, status and perspectives. *Atmospheric Chemistry and Physics*, *18*(7), 4935–4964. https://doi.org/10.5194/acp-18-4935-2018

Eyring, V., Waugh, D. W., Bodeker, G. E., Akiyoshi, H., Austin, J., Beagley, S. R., et al. (2007). Multimodel projections of stratospheric ozone in the 21st century. *Journal of Geophysical Research*, *112*(D16303). https://doi.org/10.1029/2006JD00833

Finger, F. G., Gelman, M. E., Miller, A. J., Wild, J. D., Chanin, M. L., & Hauchecorne, A. (1993). Evaluation of nmc upper-stratospheric temperature analyses using rocketsonde and lidar data. *Bulletin of the American Meteorological Society*, *74*(5), 789–799. https://doi.org/10.1175/1520-0477(1993)074<0789:EONUST>2.0.CO;2

Friedlingstein, P., Meinshausen, M., Arora, V. K., Jones, C. D., Anav, A., Liddicoat, S. K., et al. (2014). Uncertainties in cmip5 climate projections due to carbon cycle feedbacks. *Journal of Climate*, *27*(2), 511–526. https://doi.org/10.1175/JCLI-D-12-00579.1

Garcia, R. R., Marsh, D. R., Kinnison, D. E., Boville, B. A., & Sassi, F. (2007). Simulation of secular trends in the middle atmosphere, 1950–2003. *Journal of Geophysical Research*, *112*(D09301). https://doi.org/10.1029/2006JD007485

Gardiner, T., Forbes, A., de Mazière, M., Vigouroux, C., Mahieu, E., Demoulin, P., et al. (2008). Trend analysis of greenhouse gases over Europe measured by a network of ground-based remote FTIR instruments. *Atmospheric Chemistry and Physics*, *8*(22), 6719–6727. https://doi.org/10.5194/acp-8-6719-2008

Gaudel, A., Cooper, O. R., Ancellet, G., Barret, B., Boynard, A., Burrows, J. P., et al. (2018). Tropospheric ozone assessment report: Present-day distribution and trends of tropospheric ozone relevant to climate and global atmospheric chemistry model evaluation. *Elementa: Science of the Anthropocene*, *6*, 47. https://doi.org/10.1525/elementa.291

Glatthor, N., Höpfner, M., Leyser, A., Stiller, G. P., von Clarmann, T., Grabowski, U., et al. (2017). Global carbonyl sulfide (OCS) measured by MIPAS/Envisat during 2002-2012. *Atmospheric Chemistry and Physics*, *17*(4), 2631–2652. https://doi.org/10.5194/acp-17-2631-2017

Griffith, D. W. T., Jones, N. B., & Matthews, W. A. (1998). Interhemispheric ratio and annual cycle of carbonyl sulfide (OCS) total column from ground-based solar FTIR spectra. *Journal of Geophysical Research*, *103*(D7), 8447–8454. https://doi.org/10.1029/97JD03462

Gunson, M. R., Abbas, M. M., Abrams, M. C., Allen, M., Brown, L. R., Brown, T. L., et al. (1996). The atmospheric trace molecule spectroscopy (atmos) experiment: Deployment on the atlas space shuttle missions. *Geophysical Research Letters*, *23*(17), 2333–2336. https://doi.org/10.1029/96GL01569

Hase, F., Hannigan, J., Coffey, M., Goldman, A., Höpfner, M., Jones, N., et al. (2004). Intercomparison of retrieval codes used for the analysis of high-resolution, ground-based FTIR measurements. *Journal of Quantitative Spectroscopy and Radiative Transfer*, *87*, 24–52. https://doi.org/10.1016/j.jqsrt.2003.12.008

Hilton, T. W., Whelan, M. E., Zumkehr, A., Kulkarni, S., Berry, J. A., Baker, I. T., et al. (2017). Peak growing season gross uptake of carbon in north America is largest in the Midwest USA. *Nature Climate Change*, *7*(6), 450–454. https://doi.org/10.1038/nclimate3272

Kettle, A. J., Kuhn, U., von Hobe, M., Kesselmeier, J., & Andreae, M. O. (2002). Global budget of atmospheric carbonyl sulfide: Temporal and spatial variations of the dominant sources and sinks. *Journal of Geophysical Research*, *107*, 4658. https://doi.org/10.1029/2002JD002187

Kivi, R., Kyrö, E., Turunen, T., Harris, N. R. P., von der Gathen, P., Rex, M., et al. (2007). Ozonesonde observations in the arctic during 1989–2003: Ozone variability and trends in the lower stratosphere and free troposphere. *Journal of Geophysical Research: Atmospheres*, *112*(D8). https://doi.org/10.1029/2006JD007271

Kohlhepp, R., Ruhnke, R., Chipperfield, M. P., De Mazière, M., Notholt, J., Barthlott, S., et al. (2012). Observed and simulated time evolution of HCl, $ClONO_2$, and HF total column abundances. *Atmospheric Chemistry and Physics*, *12*(7), 3527–3556. https://doi.org/10.5194/acp-12-3527-2012

Kremser, S., Jones, N. B., Palm, M., Lejeune, B., Wang, Y., Smale, D., et al. (2015). Positive trends in Southern Hemisphere carbonyl sulfide. *Geophysical Research Letters*, *42*(21), 9473–9480. https://doi.org/10.1002/2015GL065879

Kremser, S., Thomason, L. W., von Hobe, M., Hermann, M., Deshler, T., Timmreck, C., et al. (2016). Stratospheric aerosol—Observations, processes, and impact on climate. *Reviews of Geophysics*, *54*(2), 278–335. https://doi.org/10.1002/2015RG000511

Krysztofiak, G., Té, Y. V., Catoire, V., Berthet, G., Toon, G. C., Jégou, F., et al. (2015). Carbonyl sulphide (OCS) variability with latitude in the atmosphere. *Atmosphere-Ocean*, *53*(1), 89–101. https://doi.org/10.1080/07055900.2013.876609

Kurylo, M. J., & Soloman, S. (1990). *United States NASA administration upper atmosphere research program and NOAA climate and global change program, network for the detection of stratospheric change: A status and implementation report*. Technical Report. NASA.

Launois, T., Belviso, S., Bopp, L., Fichot, C. G., & Peylin, P. (2015). A new model for the global biogeochemical cycle of carbonyl sulfide – Part 1: Assessment of direct marine emissions with an oceanic general circulation and biogeochemistry model. *Atmospheric Chemistry and Physics*, *15*(5), 2295–2312. https://doi.org/10.5194/acp-15-2295-2015

by the Helmholtz Society via the research program ATMO. Operation at the Rikubetsu and Tsukuba sites are supported in part by the GOSAT series project. Analyses of the Rikubetsu and Tsukuba data were carried out as part of the ISEE joint research program. The University of Wollongong operates the NDACC site at Wollongong and is funded through grants from the Australian Research Council. The NDACC FTIR station Zugspitze has been supported by the German Bundesministerium für Wirtschaft und Energie (BMWi) via DLR under Grant 50EE1711D and by the Helmholtz Society via the research program ATMO. The measurements at Reunion Island have been also supported by the Université de La Réunion and CNRS (LACy-UMR8105 and UMS3365). FTIR data of SPbU were acquired using instrumentation facilities provided by the Geomodel Research Center of SPbU Research Park. These data are taken and processed under the NDACC IRWG data protocols, they are archived at the NDACC DHF at www.ndacc.org and are available to the public.

Lee, C.-L., & Brimblecombe, P. (2016). Anthropogenic contributions to global carbonyl sulfide, carbon disulfide and organosulfides fluxes. *Earth-Science Reviews*, *160*, 1–18. https://doi.org/10.1016/j.earscirev.2016.06.005

Lejeune, B., Mahieu, E., Vollmer, M. K., Reimann, S., Bernath, P. F., Boone, C. D., et al. (2016). Optimized approach to retrieve information on atmospheric carbonyl sulfide (OCS) above the Jungfraujoch station and change in its abundance since 1995. *Journal of Quantitative Spectroscopy & Radiative Transfer*, *186*, 81–95. https://doi.org/10.1016/j.jqsrt.2016.06.001

Lennartz, S. T., Marandino, C. A., von Hobe, M., Cortes, P., Quack, B., Simo, R., et al. (2017). Direct oceanic emissions unlikely to account for the missing source of atmospheric carbonyl sulfide. *Atmospheric Chemistry and Physics*, *17*(1), 385–402.

Ma, J., Kooijmans, L. M. J., Cho, A., Montzka, S. A., Glatthor, N., Worden, J. R., et al. (2020). Inverse modelling of carbonyl sulfide: Implementation, evaluation and implications for the global budget. *Atmospheric Chemistry and Physics Discussions*, *2020*, 1–39. https://doi.org/10.5194/acp-2020-603

Mahieu, E., Zander, R., Delbouille, L., Demoulin, P., Roland, G., & Servais, C. (1997). Observed trends in total vertical column abundances of atmospheric gases from IR solar spectra recorded at the Jungfraujoch [Article]. *Journal of Atmospheric Chemistry*, *28*(1–3), 227–243. https://doi.org/10.1023/A:1005854926740

Mankin, W. G., Coffey, M. T., Griffith, D. W. T., & Drayson, S. R. (1979). Spectroscopic measurement of carbonyl sulfide (OCS) in the stratosphere. *Geophysical Research Letters*, *6*, 853–856. https://doi.org/10.1029/GL006i011p00853

Montzka, S. A., Calvert, P., Hall, B. D., Elkins, J. W., Conway, T. J., Tans, P. P., et al. (2007). On the global distribution, seasonality, and budget of atmospheric carbonyl sulfide (COS) and some similarities to $CO_2$. *Journal of Geophysical Research*, *112*(D9D09302). https://doi.org/10.1029/2006JD007665

Montzka, S. A., & Fraser, P. J. (2003). Controlled substances and other source gases. In *Scientific assessment of ozone depletion: 2002 (Vol. Scientific Assessment of Ozone Depletion: 2002, chap. 1)*. World Meteological Organization.

Notholt, J., Bingemer, H., Berresheim, H., Holton, J., Kettle, A., Mahieu, E., et al. (2006). Precursor gas measurements In L. Thomason & T. Peter (Eds.), *SPARC: Assessment of aerosol processes (ASAP)*. (pp. 29–76). World Climate Research Programme.

Notholt, J., Kuang, Z., Rinsland, C. P., Toon, G. C., Rex, M., Jones, N., et al. (2003). Enhanced upper tropical tropospheric COS: Impact on the stratospheric aerosol layer. *Science*, *300*(5617), 307–310. https://doi.org/10.1126/science.1080320

Olsen, K. S., Strong, K., Walker, K. A., Boone, C. D., Raspollini, P., Plieninger, J., et al. (2017). Comparison of the GOSAT TANSO-FTS TIR $CH_4$ volume mixing ratio vertical profiles with those measured by ACE-FTS, ESA MIPAS, IMK-IAA MIPAS, and 16 NDACC stations. *Atmospheric Measurement Techniques*, *10*(10), 3697–3718. https://doi.org/10.5194/amt-10-3697-2017

Plumb, R. A., & Ko, M. K. W. (1992). Interrelationships between mixing ratios of long-lived stratospheric constituents. *Journal of Geophysical Research*, *97*(D9), 10145–10156. https://doi.org/10.1029/92JD00450

Pougatchev, N. S., Connor, B. J., & Rinsland, C. P. (1995). Infrared measurements of the ozone vertical distribution above kitt peak. *Journal of Geophysical Research*, *100*(D8), 16689–16697. https://doi.org/10.1029/95JD01296

Randel, W. J., Shine, K. P., Austin, J., Barnett, J., Claud, C., Gillett, N. P., et al. (2009). An update of observed stratospheric temperature trends. *Journal of Geophysical Research*, *114*(D02107). https://doi.org/10.1029/2008JD010421

Rinsland, C. P., Chiou, L., Mahieu, E., Zander, R., Boone, C. D., & Bernath, P. F. (2008). Measurements of long-term changes in atmospheric OCS (carbonyl sulfide) from infrared solar observations. *Journal of Quantitative Spectroscopy & Radiative Transfer*, *109*, 2679–2686. https://doi.org/10.1016/j.jqsrt.2008.07.008

Rinsland, C. P., Goldman, A., Mahieu, E., Zander, R., Notholt, J., Jones, N. B., et al. (2002). Ground-based infrared spectroscopic measurements of carbonyl sulfide: Free tropospheric trends from a 24-year time series of solar absorption measurements. *Journal of Geophysical Research*, *107*(D22), ACH24-1–ACH24-9. https://doi.org/10.1029/2002JD002522

Rinsland, C. P., Jones, N. B., Connor, B. J., Logan, J. A., Pougatchev, N. S., Goldman, A., et al. (1998). Northern and southern hemisphere ground-based infrared spectroscopic measurements of tropospheric carbon monoxide and ethane. *Journal of Geophysical Reasearch*, *103*, 28197–28217.

Rodgers, C. D. (1976). Retrieval of atmospheric temperature and composition from remote measurements of thermal radiation. *Reviews of Geophysics*, *14*(4), 609–624. https://doi.org/10.1029/RG014i004p00609

Rodgers, C. D. (1990). Characterization and error analysis of profiles retrieved from remote sounding measurements. *Journal of Geophysical Research*, *95*(D5), 5587–5595. https://doi.org/10.1029/JD095iD05p05587

Rodgers, C. D. (1998). Information content and optimisation of high spectral resolution remote measurements. *Advances in Space Research*, *21*, 361–367.

Rodgers, C. D. (2000). *Inverse methods for atmospheric sounding*. World Scientific Publishing Co. Pte. Ltd.

Rothman, L., Gordon, I., Babikov, Y., Barbe, A., Benner, D. C., Bernath, P., et al. (2013). The HITRAN 2012 molecular spectroscopic database. *Journal of Quantitative Spectroscopy and Radiative Transfer*, *130*, 4–50. https://doi.org/10.1016/j.jqsrt.2013.07.002

Sheng, J.-X., Weisenstein, D. K., Luo, B.-P., Rozanov, E., Stenke, A., Anet, J., et al. (2015). Global atmospheric sulfur budget under volcanically quiescent conditions: Aerosol-chemistry-climate model predictions and validation. *Journal of Geophysical Research: Atmospheres*, *120*(1), 256–276. https://doi.org/10.1002/2014JD021985

Stinecipher, J., Cameron-Smith, P., Blake, N., Kuai, L., Lejeune, B., Mahieu, E., et al. (2019). Biomass burning unlikely to account for missing source of carbonyl sulfide. *Geophysical Research Letters*, *46*(24), 14912–14920. https://doi.org/10.1029/2019GL085567

Stolarski, R. S., Douglass, A. R., & Strahan, S. E. (2018). Using satellite measurements of $n_2o$ to remove dynamical variability from HCL measurements. *Atmospheric Chemistry and Physics*, *18*(8), 5691–5697. https://doi.org/10.5194/acp-18-5691-2018

Suntharalingam, P., Kettle, A. J., Montzka, S. M., & Jacob, D. J. (2008). Global 3-D model analysis of the seasonal cycle of atmospheric carbonyl sulfide: Implications for terrestrial vegetation uptake. *Geophysical Research Letters*, *35*, L19801. https://doi.org/10.1029/2008GL034332

Thomason, L., & Peter, T. (2006). *SPARC: Assessment of aerosol processes (ASAP) (Technical Report)*. World Climate Research Programme.

Toon, G. C., Blavier, J.-F. L., & Sung, K. (2018). Atmospheric carbonyl sulfide (OCS) measured remotely by FTIR solar absorption spectrometry. *Atmospheric Chemistry and Physics*, *18*(3), 1923–1944. https://doi.org/10.5194/acp-18-1923-2018

Turco, R. P., Whitten, R. C., Toon, O. B., Pollack, J. B., & Hamill, P. (1980). OCS, stratospheric aerosols and climate. *Nature*, *283*(5744), 283–285. https://doi.org/10.1038/283283a0

Velazco, V. A., Toon, G. C., Blavier, J.-F. L., Kleinböhl, A., Manney, G. L., Daffer, W. H., et al. (2011). Validation of the atmospheric chemistry experiment by noncoincident MkIV balloon profiles. *Journal of Geophysical Research*, *116*(D6D06306). https://doi.org/10.1029/2010JD014928

Vigouroux, C., Aquino, C. A. B., Bauwens, M., Becker, C., Blumenstock, T., Mazière, M. D., et al. (2018). NDACC harmonized formaldehyde time-series from 21 FTIR stations covering a wide range of column abundances. *Atmospheric Measurement Techniques*, *11*(9), 5049–5073. https://doi.org/10.5194/amt-11-5049-2018

Vigouroux, C., Blumenstock, T., Coffey, M., Errera, Q., García, O., Jones, N. B., et al. (2015). Trends of ozone total columns and vertical distribution from FTIR observations at eight NDACC stations around the globe. *Atmospheric Chemistry and Physics*, *15*(6), 2915–2933. https://doi.org/10.5194/acp-15-2915-2015

Vigouroux, C., Mazière, M. D., Demoulin, P., Servais, C., Hase, F., Blumenstock, T., et al. (2008). Evaluation of tropospheric and stratospheric ozone trends over Western Europe from ground-based FTIR network observations. *Atmospheric Chemistry and Physics*, *8*, 6865–6886.

Wang, Y., Deutscher, N. M., Palm, M., Warneke, T., Notholt, J., Baker, I., et al. (2016). Towards understanding the variability in biospheric $CO_2$ fluxes: Using FTIR spectrometry and a chemical transport model to investigate the sources and sinks of carbonyl sulfide and its link to $CO_2$. *Atmospheric Chemistry and Physics*, *16*(4), 2123–2138. https://doi.org/10.5194/acp-16-2123-2016

Whelan, M. E., Lennartz, S. T., Gimeno, T. E., Wehr, R., Wohlfahrt, G., Wang, Y., et al. (2018). Reviews and syntheses: Carbonyl sulfide as a multi-scale tracer for carbon and water cycles. *Biogeosciences*, *15*(12), 3625–3657. https://doi.org/10.5194/bg-15-3625-2018

Wild, J. D., Gelman, M. E., Miller, A. J., Chanin, M. L., Hauchecorne, A., Keckhut, P., et al. (1995). Comparison of stratospheric temperatures from several lidars, using national meteorological center and microwave limb sounder data as transfer references. *Journal of Geophysical Research*, *100*(D6), 11105–11111. https://doi.org/10.1029/95JD00631

Wilks, D. S. (2011). *Statistical methods in the atmospheric sciences* (3rd ed.). Elsevier.

Wofsy, S. C. (2011). Hiaper pole-to-pole observations (HIPPO): Fine-grained, global-scale measurements of climatically important atmospheric gases and aerosols. *Philosophical Transactions of the Royal Society A: Mathematical, Physical and Engineering Sciences*, *369*(1943), 2073–2086. https://doi.org/10.1098/rsta.2010.0313

Wofsy, S. C., Daube, B. C., Jimenez, R., Kort, E., Pittman, J. V., Park, S., et al. (2017). *HIPPO combined discrete flask and GC sample GHG, halocarbon, hydrocarbon data version 1.0*. (R20121129) (Technical Report). UCAR/NCAR—Earth Observing Laboratory. https://doi.org/10.3334/CDIAC/hippo_012

Wohltmann, I., Lehmann, R., Rex, M., Brunner, D., & Mäder, J. A. (2007). A process-oriented regression model for column ozone. *Journal of Geophysical Research*, *112*(D12). https://doi.org/10.1029/2006JD007573

Zander, R., Rinsland, C. P., Farmer, C. B., Namkung, J., Norton, R. H., & Russell, J. M., III. (1988). Concentrations of carbonyl sulfide and hydrogen cyanide in the free upper troposphere and lower stratosphere deduced from atmos/spacelab 3 infrared solar occultation spectra. *Journal of Geophysical Research*, *93*(D2), 1669–1678. https://doi.org/10.1029/JD093iD02p01669

Zängl, G., & Hoinka, K. P. (2001). The tropopause in the polar regions. *Journal of Climate*, *14*(14), 3117–3139. https://doi.org/10.1175/1520-0442(2001)014<3117:TTITPR>2.0.CO;2

Zhou, M., Langerock, B., Wells, K. C., Millet, D. B., Vigouroux, C., Sha, M. K., et al. (2019). An intercomparison of total column-averaged nitrous oxide between ground-based FTIR TCCON and NDACC measurements at seven sites and comparisons with the GEOS-Chem model. *Atmospheric Measurement Techniques*, *12*(2), 1393–1408. https://doi.org/10.5194/amt-12-1393-2019

Zumkehr, A., Hilton, T. W., Whelan, M., Smith, S., Kuai, L., Worden, J., et al. (2018). Global gridded anthropogenic emissions inventory of carbonyl sulfide. *Atmospheric Environment*, *183*, 11–19. https://doi.org/10.1016/j.atmosenv.2018.03.063